Compaction effects on evaporation and salt precipitation in drying porous media

Nurit Goldberg [1,2], Shmuel Assouline [1], Yair Mau [2], Uri Nachshon [1]

[1]Institute of Soil, Water and Environmental Sciences, Agricultural Research Organization-Volcani Institute, Rishon Lezion 7505101, Israel

[2]The Institute of Environmental Sciences, The Robert H. Smith Faculty of Agriculture, Food and Environment, The Hebrew University of Jerusalem, Rehovot 7610001, Israel

Correspondence to: Uri Nachshon (urina@agri.gov.il)

Abstract

Compaction and salinization of soils reduce croplands fertility, affect natural ecosystems, and are major concerns worldwide. Soil compaction alters soil structure and affects the soil's hydraulic properties. It therefore may have a significant impact on evaporation and solute transport processes in the soil. In this work, we investigated the combined processes of soil compaction, bare soil evaporation, and salt precipitation. X-ray computed micro tomography techniques were used to study the geometrical soil pore and grain parameters influenced by compaction. The impact of compaction on evaporation and salt precipitation was studied using column experiments. We found that compaction reduced the average grain size and increased the number of grains, due to the crushing of the grains and their translocation within the compacted soil profile. Changes in pore and grain geometry and size were heterogeneously distributed throughout the soil profile, with changes most apparent near the source of compaction, in our case, at the soil surface. The column experiments showed that the presence of small pores in the upper layer of the compacted soil profile leads to higher evaporation losses and salt precipitation, due to the increase of hydraulic connectivity to the soil surface and the prolongation of the first stage of evaporation.

1. Introduction

Soil compaction is a major cause of soil degradation in agricultural environments (Akker and Canarache, 2001; Hamza and Anderson, 2005; Pagliai et al., 2003). It is associated with the increase of soil bulk density and decrease of porosity (Mossadeghi-Björklund et al., 2016). Soil compaction at different intensities may occur due to natural processes such as the impact of raindrops, natural soil-forming processes, animal treading, and to processes linked to human activities, especially in agricultural environments, such as intense vehicular traffic over the fields (Assouline, 2004; Pagliai et al., 2003; Shah et al., 2017; Mossadeghi-Björklund et al., 2018). Passing of heavy machinery and vehicles over the fields leads to compaction as a result of pure static stresses, wheel slip and dynamic forces, caused by vibration of the engine and the attached implements (Horn et al., 1995). Barik et al. (2014) found significant variability in the spatial distribution of the aggregate stability, bulk density, total porosity, penetration resistance, and moisture content values, following traffic operation over arable lands. Pores nearby the location of compression are strongly affected, whereas those located further away from the source of compaction are less affected (Schlüter and Vogel, 2016; Keller et al., 2019). Thus, compaction resulting from traffic generally presents a sigmoidal distribution with depth of the soil bulk density, where the denser part is close to the surface (Reicosky et al., 1981; Horton et al., 1994; Dejong-Hughes et al., 2001; Assouline, 2004; Bresson et al., 2004; Augeard et al., 2007).

To overcome soil compaction in arable lands and to loosen up the soil upper layer, soil tillage is implemented, producing favorable conditions for seed germination and crop root development. Soil tillage reduces soil bulk density, increases porosity, homogenizes soil-wetting processes and improves soil aeration in the root zone (Rasmussen, 1999; El Titi, 2003; Assouline et al., 2014; de Almeida et al., 2018). On the other hand, under certain conditions,

2

tillage may accelerate processes of soil erosion and compaction of the soil at the lower

55   boundary of the tilled zone (de Almeida et al., 2018), i.e., the plough pan (Podder et al., 2012).

Therefore, minimizing vehicles passing over the fields, reducing tillage, and improving our

understanding of the nature of soil compaction is important.

1.1. Soil compaction at the micro-scale

At the microscale, stresses in soil do not propagate homogeneously but rather through

60   preferential paths – in all directions (Nawaz et al., 2013). Consequently, soil deformation

occurs at specific sites, where the stresses and strains are maximal. These areas, known also

as shear bands, are those that undergo structural deformation, while soil volumes in between

the stress chains may preserve their original structure and porosity (Nawaz et al., 2013;

Naveed et al., 2016). The heterogeneous effect of compaction on the physical properties of

65   the soil leads to an uneven spatial distribution of the soil's hydraulic properties that in turn

affect water flow and solute transport processes in the soil profile (Assouline, 2006a; b;

Assouline and Or, 2006; Alaoui et al., 2018).

Soil compaction affects the pore network in the soil profile, with respect to: (i) pore-size

distribution; (ii) pore geometry and morphology; and (iii) pore connectivity (Horn et al., 1995;

70   Mossadeghi-Björklund et al., 2016). Consequently, water-related soil properties are

significantly altered (Horn et al., 1995; Assouline, 2006a; b). These changes affect unsaturated

soil hydraulic properties and reduce saturated soil hydraulic conductivity, thus increasing

surface runoff and soil erosion by water (Soane and van Ouwerkerk, 1995; Alaoui et al., 2011;

Keller et al., 2013; Shah et al., 2017). In addition, soil aeration is reduced and the

75   heterogeneous changes of the soil's physical and hydrological properties, may lead to the

formation of preferential water flow paths in the soil (Soane and van Ouwerkerk, 1995; Alaoui

et al., 2011; Keller et al., 2013). Consequently, solute transport and accumulation in the soil

may be affected, impacting nutrient availability to plants (Horn et al., 1995; Lipiec and

Stępniewski , 1995; Hendrickx and Flury, 2001; Mossadeghi-Björklund et al., 2016). The above-mentioned changes of the soil properties, due to compaction, usually occur at the top 30 cm of the soil profile (Horn et al., 1995; Keller et al., 2019). These changes in the soil structure of the upper soil layer impacts on the soil water balance in general, and on infiltration and evaporation processes in particular (Sillon et al., 2003; Assouline et al., 2007, 2014; Shokri et al., 2010).

1.2. Bare soil evaporation

Evaporation plays a central role in the hydrologic cycle and surface energy balance (Bergstad et al., 2018) as it is the main process of soil-water transfer to the atmosphere (Hillel, 1980; Brutsaert, 2005). The evaporation in porous media is affected by and involves complex and highly dynamic interactions between boundary conditions, liquid flow and vapor diffusion (Lehmann et al., 2008; Or et al., 2013; Assouline et al., 2014; Kamai and Assouline, 2018; Assouline and Kamai, 2019).

The evaporation process from bare soils consists of two stages: stage 1 (S1) and stage 2 (S2). Evaporation during S1 takes place at the soil surface, and a hydraulic connection is maintained throughout the soil profile, by capillary flow of water through the soil's small pores (Lehmann et al., 2008; Nachshon et al., 2011a; b; Bergstad et al., 2018; Assouline and Narkis, 2019). In parallel to the upward capillary flow, through the small pores, the larger pores in the soil are air invaded. The interface between saturated and partially dry regions is defined as the drying front (Shokri et al., 2008). S1 is characterized by a high and relatively constant evaporation rate affected by soil properties and atmospheric conditions (Hillel, 1980). S2 begins when a characteristic capillary head, ψ_c, is reached at the soil surface, thus the small pores are air invaded, and the hydraulic connection between the soil profile and the surface is lost (Prat, 2002; Lehmann et al., 2008; Assouline et al., 2014). The evaporation front, that is the upper boundary of the capillary rise through the small pores (Shokri et al., 2008), migrates

4

downward, and evaporation rate is drastically reduced as vapor diffusion from the
105 evaporation front to the atmosphere governs the process (Lehmann et al., 2008; Nachshon et al., 2011b; Or et al., 2013; Kamai and Assouline, 2018).

Over the recent years, several works have shown that soil structure has great effect on bare soil evaporation. Lehmann et al. (2008), and following works (e.g., Lehmann and Or, 2009; Nachshon et al., 2011a, b) have shown that heterogeneous structure of the porous media,
110 consisting of two texturally different matrices (coarse and fine) separated by a sharp interface perpendicular to the evaporation front, results in elongation of S1 and increased cumulative evaporation. In short, this is a result of the large pores of the coarse media that are being invaded by air much before the fine pores, with the lower (more negative) air entry pressure. The pressure head differences between the large and fine pores results in that the coarse
115 texture domain supply water, by capillary flow, to the fine texture domain, thus more water are available for S1, through the fine pores (Lehmann and Or, 2009).

In addition, structural changes of the soil along the vertical axis (with depth), may also affect evaporation (e.g., Or et al., 2007; Lehmann et al., 2008; Assouline et al., 2014; Assouline and Narkis, 2019). It was shown that porous media composed of a fine texture domain that
120 overlies a coarse texture domain may result in longer duration of S1 and increased cumulative evaporation. In this layered structure, as soon as the drying front reaches the layers with the relatively larger pores, a rapid water displacement will occur from the large pores to the overlying finer pores. The pressure in the coarse layer changes abruptly from its air-entry value to the air-entry value at the evaporation front, which is associated to the higher capillary
125 suction of the small pores (Or et al, 2007). Consequently, the coarse texture layer acts as a water reservoir that supply extra water to sustain a longer S1 and higher cumulative evaporation, compare to a homogeneous soil structure. Important to emphasize that this process will take action only if the thickness of the fine texture layer is shorter than its ψ_c, as

only at this state the drying front may reach the coarse texture domain, while the system is in

130   S1 and evaporation front is at the soil surface (Assouline et al., 2014; Assouline and Narkis, 2019).

1.3. Evaporation and soil salinization

Evaporation and soil salinization are tightly connected processes, especially in cultivated fields. Soil salinization in cultivated fields is a common feature resulting from low-quality

135   irrigation water, fertilization, and saline and shallow groundwater resulting from inadequate irrigation and drainage practices (Yakirevich et al., 2013; Berezniak et al., 2018; Nachshon, 2018; Hopmans et al., 2021).

The presence of salts in the soil pore water reduces the osmotic potential of the solution and the equilibrium water vapor pressure (Nassar and Horton, 1997). Consequently, evaporation

140   rates from a saline soil are expected to be lower compared to solute-free conditions. During evaporation, the concentration of the dissolved ions increases in the pore solution, until saturation is reached and salt precipitation begins (Nachshon et al., 2011a). Salt precipitation at the soil surface occurs mainly during S1, where the evaporation rate is maximal and solutes are continuously transported to the evaporation front at the soil surface by capillary flow. As

145   the salt begins to precipitate and expands over the soil surface, the evaporation rate is affected by the pore-scale dynamics of the precipitated salt (Bergstad et al., 2017, 2018), and the consequent changes to liquid and vapor flow processes through the salt crust. The presence of porous media heterogeneities (Lehmann and Or, 2009; Nachshon et al., 2011b), initial solute concentration of the pore water (Rad and Shokri, 2012; Shokri-Kuehni et al.,

150   2017), soil surface properties (Nachshon et al., 2011a) and salt type (Shokri-Kuehni et al., 2017) may affect the dynamics of the salt precipitation layer and its influence on evaporation (Bergstad et al., 2018). In some cases, if the precipitated salt layer over the soil surface is hydraulically connected to the solution in the pores below, it may accelerate evaporation, as

the surface area of the precipitated salt is usually higher compared to the underlying bare soil.

155 Consequently, as long as the salt crust can pump liquid water from the underlying media, the elevated surface area of the salt crust would increase total evaporation (Shokri-Kuehni et al., 2017). On the other hand, if the precipitated salt layer is hydraulically disconnected from the solution in the pores, it acts as a barrier that reduces vapor diffusion from the soil to the atmosphere, and cumulative evaporation and evaporation rates will be reduced (Nachshon et

160 al., 2011b).

Previous studies have shown that changes in soil structure, which affect evaporation, influence also the nature and location of salt precipitation in the presence of saline solution (Nachshon et al., 2011b; a; Bergstad et al., 2017). The drying patterns and dynamics are greatly influenced by the presence of textural discontinuities that may result in preferential drying

165 and promotion of capillary exchange between different regions in the soil (Lehmann and Or, 2009; Bergstad et al., 2017). As aforementioned, soil compaction affects soil structural and textural properties, mainly at the soil surface, where evaporation and salt precipitation are prominent.

1.4. Evaporation and soil compaction

170 Studies on the effect of soil compaction on evaporation, in general, and its relation to salt precipitation in particular, are scarce. Nassar and Horton (1999) examined salinity and compaction effects on soil water evaporation from bare soils, focusing on water and solute distributions in the soil. They showed that compaction increases cumulative evaporation, due to increased matric suction of the compacted soil, resulting in the increase of the soil water

175 holding capacity and unsaturated hydraulic conductivity. Consequently, water flows more efficiently from deep parts of the soil profile to the soil surface, where evaporation is maximal, at S1 evaporation. In their study, Nassar and Horton (1999) deliberately compacted the soil samples in a homogeneous manner, ignoring the heterogeneous nature of soil compaction.

Moreover, while the authors examined the impact of compaction and evaporation on solute distribution in the soil profile, and its impact on the solution osmotic potential, they did not consider the interactions between soil compaction, evaporation, and salt precipitation.

Sillon et al. (2003), using indirect measurements under non-saline field conditions, also pointed at higher evaporation from compacted soils. The authors showed that for compacted soils, soil drying occurred from bottom to top, in opposition to regular evaporative conditions, where the drying front recedes from the surface downward. In agreement with Nassar and Horton (1999), this was explained by the high capillary suction of the compacted soil that enabled pumping of water from the lower parts of the soil profile to the soil surface, where evaporation takes place. Assouline and Narkis (2019) used a constructed multilayered porous medium, where the top layer had the highest bulk density, smallest grains, and smallest pores, and where the bulk density gradually decreased, while grains and pore sizes gradually increased in the underlying layers. They have measured evaporation from this structure and from a structure where the order of the layers was reversed. It was shown that the soil structure where the top layer had the highest bulk density extended the S1 duration and increased the cumulative evaporation in comparison to the reversed structure. The concept of the characteristic length was applied to explain these results, providing a physically-based support to the observations of Sillon et al. (2003).

The main objective of the work presented herein is to understand the impact of soil compaction on soil evaporation, solute distribution and salt precipitation, and their interactions, along the soil profile. Relying on previous works (Nassar and Horton, 1999; Sillon et al., 2003; Assouline and Narkis, 2019), we conducted a series of experiments to fill up the knowledge gaps regarding the complex interactions between the heterogeneous structural nature of compacted soils, evaporation, and salt dynamics.

8

2. Conceptual model

Based on the studies detailed above, we hypothesize that compacted soil may be considered as a semi-layered structure where pores openings are minimal at the soil surface, due to compaction, and gradually increase with depth (**Figure 1A**). Consequently, soil bulk density, capillary suction, water holding capacity and unsaturated hydraulic conductivity are maximal at the upper layer of the soil profile, as well as its characteristic capillary length. These structural changes will result in evaporation patterns similar to those observed for the layered structure domain with fine media overlies a coarser texture domain.

It is hypothesized that for compacted conditions the first tip of the drying front that will invade the underlying larger pores, will act as an air conduit that will allow air to replace the water that will be pumped upward by the fine texture horizons (**Figure 1B(2)**). Consequently, at the compacted soil scenario, during evaporation, the upper layers of the medium will retain high levels of saturation, while the matrix will be dried from bottom to top. This will lead to higher cumulative evaporation and longer S1, compare to the non-compacted state.

Under saline conditions, where the pores are filled with a salty solution, evaporation will lead to solute precipitation at the soil surface, and to the formation of an efflorescence salt crust, at least in the case of NaCl (Nachshon and Weisbrod, 2015; Piotrowski et al., 2020). At the non-compacted conditions, the receding drying front during evaporation and the resulted increased matric potential and reduction of the soil water content near the soil surface, will results in a quick transition into a state of a hydraulic discontinuity between the soil and the salt crust. Therefore, the salt crust will reduces evaporation as it acts as a barrier for water vapor diffusion from the evaporation front to the atmosphere (**Figure 1B(1)**). On the other hand, in the compacted soil condition, it is hypothesized that the drying pattern from bottom to top and the high water saturation that is sustained near the soil surface, will maintain a

230 Therefore, it is hypothesized

that even though more salt is expected to accumulate on the surface of the compacted soil,

due to the higher evaporation, its impact on evaporation will be moderate compared to non-

compacted conditions.
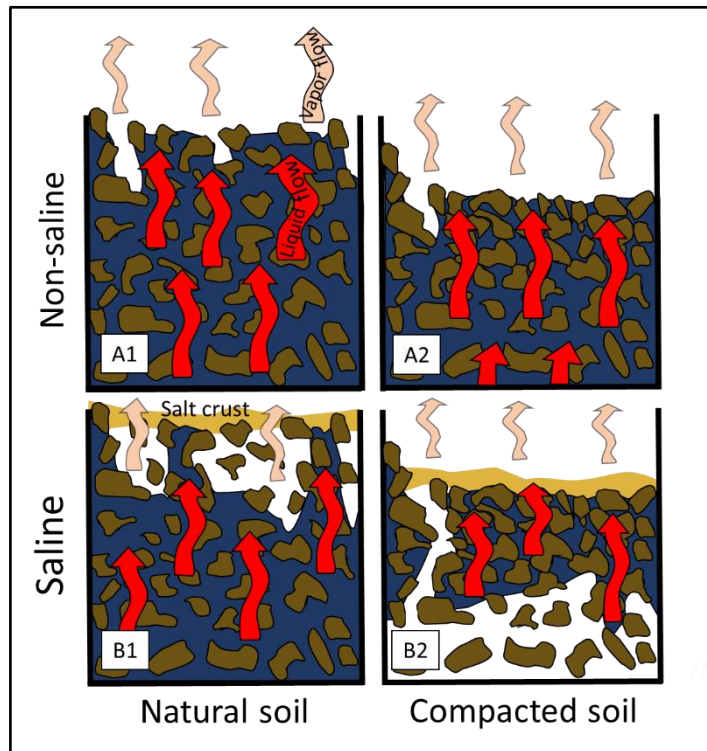
235 **Figure 1: Conceptual model of evaporation and salt precipitation under compacted and non-
     compacted conditions; (A) initial stages of S1 evaporation with the first air invasion into the
     matrix. (B) advanced stages of evaporation, where most of the soil is hydraulically
     disconnected from the salt crust for the non-compacted state (B1), whereas at the
     compacted state, most of the soil is hydraulically connected to the salt crust, thus**
240 **evaporation front is at the salt crust upper surface (B2). Drying of the compacted media is
     from bottom to top, as liquid water is replaced by air that is flowing downward through the
     larger pores that act as air conduits.**

These hypotheses were tested herein by means of high-resolution micro CT scans, to

characterize, at the micro scale, the impact of compaction on soil pores and grains properties,

245 and column experiments to study the impact of compaction, at the macro-scale, on

evaporation and salt precipitation. A simple numerical model was used also, to strengthen

some aspects of the experimental findings and research hypotheses.

3. Materials and method

This study relies on three parts: (i) studying the impact of compaction on soil physical properties at the micro and macro scales; (ii) simple numerical simulation of evaporation from a layered domain, mimicking compacted and loose porous media, with and without the presence of a precipitated salt crust; and (iii) validation of the conceptual model presented in **Figure 1** by means of macro scale evaporation experiments, for compacted and layered domains.

3.1. Micro scale changes of pores and grains physical properties due to compaction

Imaging of sand samples before and after compaction was conducted in a non-destructive manner using a high-resolution µCT (SKYSCAN 1172, Bruker, Kontich, Belgium), in order to observe the impact of compaction on the sand physical structure, pores and grains dimensions, and spatial arrangement. The X-ray source voltage was 80 kV, and the electrical current, 10 mAs. The scan was done with aluminum and copper filters, with image rotation of 0.2°. Images with voxel resolution of 4.42 µm were reconstructed by the software 'NRecon' (Bruker, Kontich, Belgium). Image analyses were carried out using designated MATLAB codes, the software 'CT-vox' (Bruker, Kontich, Belgium) and the open source image analysis software, ImageJ (Collins, 2007).

Polyvinyl chloride (PVC) tubes, 3-cm-long and 1.6-cm in diameter, open at the top and sealed at the bottom, were filled with quarry coarse sand (quartz), with mean grain diameter of ~500 µm (sand characteristics can be found in Nachshon, 2016). The columns were scanned before and following mechanical compaction, in order to detect the impact of compaction on microscale changes of the sand properties, as a function of depth and distance from the source of compression. Compaction was achieved using a PVC shaft that fits exactly the inner diameter of the column. The shaft was slowly pushed downward to compress the sand samples, using a hand-operated press, achieving a one-dimensional confined compression.

11

The samples were compressed down to a decrease of the total length of the sand sample by 2 mm, corresponding to an increase of ~7% of the packing bulk density of the samples.

275   The images from the µCT scans were used to analyze grain and pore sizes at the top 7 mm of the sand samples and at depth of 9-18 mm. Hereafter, the top and lower levels of the compacted samples will be referred to as 'TC' and 'LC', respectively, and the non-compacted control will be referred to as 'UN'. The TC and LC results were used to compare the impact of compaction at the top and the lower layers of the sample. Each µCT scan generates hundreds

280   of images of 2D slices of the sample, with a 4.42 µm distance between adjacent slices. For each scan, five 2D images, out of the hundreds of images, were chosen randomly, processed, and analyzed by a MATLAB code.

Grayscale calculations were based on Otsu's method, which selects the threshold to minimize the interclass variance (Otsu, 1979). Morphological operations were done to clean image

285   noises. Grain counting and grain area calculations were done using the function '*regionprops*', at the MATLAB - Image Processing Toolbox. A distance heat map was generated using the Euclidean distance transform, '*bwdist*' and the function '*bwskel*', both from the MATLAB - Image Processing Toolbox. Pore sizes were obtained by calculating the average maximal pore distance from the closest grain edge along the pores and throats. Grain distribution map was

290   generated by counting the center of each grain. Size based segmentation and visualization of the sand grains was done using the 'Analyze Particles' function in ImageJ.

3.2. Macro scale changes at the soil profile due to compaction

While the µCT experiments described above were used to study the effect of compaction at the pore scale, a transparent 10 cm long and 5 cm in diameter PVC column was used to

295   examine the effect of compaction at the macro scale. The same coarse sand as detailed above was used in this experiment. To allow visual observation of changes in the compacted sand

column, 10% of the sand (by weight) was colored with a standard red spray paint. The colored sand was thoroughly mixed with the regular sand, before packing the column.

As described previously, the sand in the column was compacted by decreasing the total length
300   of the sand sample by 5 mm, using a uniform hammer beating on a circular shaft, with the same diameter as the inner diameter of the PVC column. The bulk density of the sand sample was increased by ~5% following compaction.

Pictures of the sand column profile were taken before and after compaction by a single lens reflex camera (Canon - EOS60D, Japan), with an EFS18-200 mm lens (Japan). Compaction was
305   evaluated by visual analysis of the images that captured the movement of the colored sand grains and measuring the translocation of the same colored grains before and after compaction.

3.3. Numerical model

A preliminary analysis, and to estimate the general impact of soil compaction on
310   evaporation, with and without the presence of a precipitated salt crust, was carried out based on simulations using HYDRUS-1D (Šimůnek et al., 2013). Under the assumption that compacted soil is most affected at the soil surface, where compression forces are maximal, the simulated compacted domain was composed of five discrete layers, 2 cm each, where the most upper layer had the smallest grain diameter, lowest saturated hydraulic
315   conductivity and highest air entry pressure. Underlying layers were gradually comprised of bigger particles, higher hydraulic conductivity and lower air entry pressure, as detailed in **Table 1**. For the neutral domain, the same particles that were selected to compose the discrete layers of the compacted domain were homogeneously mixed and its hydraulic properties are detailed in **Table 1** also.

320   The sizes of the particles at the different modeled layers were determined upon real physical sizes of glass beads that were used in the column experiments that will be presented in the

next section. Saturation water content, θ_s, was determined experimentally by measuring the volume of water needed to saturate the different glass beads that were packed in a known volume. In order to enable a complete drying of the media, by evaporation, $\theta_r = 0$ was

325   selected, as recently done by Zhou et al. (2021). Nevertheless, the model was tested for θ_r values in the range of 0-0.05, and for all θ_r values the simulated results were consistent, with small differences in cumulative evaporation (< 10%) and identical trends of water content and pressure head profiles. The van Genuchten parameter α was determined according to Benson et al. (2014) that correlated α to particles diameter. The van-Genuchten n parameter

330   is affected by the degree of grain uniformity in the domain (Wang et al., 2017), where high n values indicate on high uniformity. Therefore, n was taken as 3 for the uniform layers, as it was the highest n value permitted by HYDRUS, while keeping the relative error in the water mass balance of the entire flow domain, at low values at the order of 1% and below. For the homogeneously mixed domain, n was arbitrarily chosen to be equal to 1.25 as the medium

335   was composed of particles with various sizes. Hydraulic conductivity at saturation, K_s [cm/d], was determined by the Kozeny-Carman equation (Kozeny, 1927; Carman, 1937), as demonstrated by Weisbrod et al. (2013)

Table 1: Hydraulic parameters for the HYDRUS-1D modeled glass beads.

Modeled domain	Depth [mm]	Particles diameter [mm]	Residual water content θ_r [-]	Saturation water content θ_s [-]	Van-Genuchten parameters α [1/cm]	n [-]	Hydraulic conductivity K_s [cm/d]
Compacted	0-20	0.049 – 0.053	0	0.39	0.01	3	232.5
	20-40	0.090 – 0.106	0	0.36	0.02	3	578.7
	40-60	0.180 – 0.212	0	0.38	0.03	3	2922.9

14

	60-80	0.400 – 0.500	0	0.29	0.07	3	5654.9
	80-100	1.000 – 1.300	0	0.41	0.15	3	14613.9
Non-compacted	0-100	Homogeneous mixing of all beads	0	0.28	0.05	1.25	3537.9
Salt crust	Thickness of 2 mm	--------------	0	0.41	0.124	2.28	350.2

340

The modeled domains had a depth of 10 cm and the upper boundary condition was set as atmospheric boundary, with potential evaporation of 0.65 cm/d (based on the data obtained in the laboratory glass-beads evaporation experiment, which will be detailed below). Lower boundary was set as zero flux and initial condition was set as full saturation throughout the entire column. Since HYDRUS solves the Richards equation, its results are valid only during S1 where evaporation is occurring at the soil surface and there is a hydraulic continuity along the soil profile. Therefore, simulations were ceased once S1 was ended and the transition to S2 begun.

The simulations were used to observe changes of the soil profile wetness and to compute cumulative evaporation for the compacted and neutral setups, with and without the presence of a salt crust. The salt crust was simulated by adding a 2 mm layer on top of the modeled domains (this thickness is similar to the observed one corresponding to the depositing salt layers during the experiments presented below). This layer was added after two days of evaporation, as it is experimentally known that the appearance of the salt crust is not instantaneous with the onset of evaporation. The hydraulic properties of a salt layer are unknown, excluding permeability, k, which was recently examined, and found to be at the order of 4×10^{-12} m^2, for NaCl (Nachshon and Weisbrod, 2015; Piotrowski et al., 2020).

345

350

355

The permeability was used to calculate the saturated hydraulic conductivity of the salt, by the relation between K_s and k (Kasenow, 2002):

360 $\quad K_S = \frac{k \cdot \rho \cdot g}{\mu}$ (1)

where μ [kg/ms] is the dynamic viscosity; ρ [kg/m^3] is the liquid density; and g [m/s^2] is gravity acceleration. For water, ρ = 1000 kg/m^3, and $\mu \sim$ 0.0009 kg/ms (at 25°c). g = 9.8 m/s^2, and for the NaCl permeability of 4 × 10^{-12} m^2 K_s is equal to 4.3 × 10^{-5} m/s = 376.0 cm/d. Since no further information is available about the salt hydraulic properties, the van-Genuchten

365 parameters of the salt layer were taken to be equal to loamy-sand soil, from the HYDRUS-1D library, due to the similar hydraulic conductivity that this soil (350.2 cm/d) has to the salt layer. Important to emphasize is that the model examined only the physical impact that a salt crust has on water flow process during S1 and did not account for the chemical aspects of high salinity and associated changes of the solution osmotic potential, surface tension and

370 viscosity.

Upper boundary condition of the simulated salt layer was as defined or the salt free setup, with atmospheric potential evaporation of 0.65 cm/day. Initial pressure head of -1000 cm was defined for the added salt layer, assuming it is dryer than the underlying soil. Model sensitivity to the initial pressure head of the salt crust was low, as it was tested for various

375 levels in the range of -1000 to -100 cm and simulation results were identical, as after one time step the pressure head of the salt crust and resultant water content were adjusted in respect to the wetness of the underlying soil. Important to emphasize that the model was tested also for a more moderate change of the soil hydraulic properties, where the hydraulic properties of the five layers (**Table 1**) were interpolated, and evenly distributed, over 30

380 layers, 3 mm each. Results of the five layers and the 30 layers' structures were similar, hence hereon only the results of the five layers will be discussed, as it corresponds to the experimental setup.

3.4. Impact of compaction on evaporation and salt precipitation

Two sets of column-evaporation experiments were conducted: (i) constructed layered structures of glass beads, in known dimensions and physical properties; and (ii) compacted and non-compacted coarse sand. The glass beads experiments aimed to test the research hypothesis under synthetic and controlled conditions, whereas the coarse sand column experiments aimed to correlate the layered structure experiments and findings to regular compaction conditions.

The layered glass beads evaporation experiments were conducted on rectangular glass columns, 10 cm high, 5 cm width, and 2.5 cm aperture. The neutral (uncompacted) and compacted columns were packed with glass beads of different sizes and different arrangements, as detailed in **Table 1**. In this set of experiments, a setup of tilled soil was examined also, and for this purpose the tilled setup was constructed in a reverse order of the compacted setup, with the largest glass beads at the top of the profile and the smallest beads at the bottom.

The three different setups were saturated with distilled water (DI) or with a 10% (by weight) NaCl solution. All the evaporation experiments were carried out in two replicates. The packed columns were positioned on high resolution electronic scales (±0.01 gr, Adam; Shekel, Israel) in order to record mass changes, thus monitoring the cumulative water loss to evaporation. Small fans (Y.S. TECH, DC BRUSHLESS FAN, FD128020HB, DC12V, 0.15V) were installed ~3 cm above the upper soil surfaces of the samples, pulling air upward. Along the process of evaporation, photos of the columns profiles were taken with a camera (UEye, Germany) at a rate of 6 pictures per minute. Total duration of evaporation for each setup was about 12.5 days (~303 hours).

The coarse sand experiments were conducted in circular columns, 92 cm long and 4.1 cm in diameter. The columns were filled with the same coarse sand used for the CT scans

410

415

4. Results and Discussion

Experimental results are organized and presented first, for the micro-scale, and then for the macro scale; considering the physical changes that the sand underwent due to compaction. Following that, the results representing the impact of compaction on the combined processes

420 of evaporation and salt precipitation will be discussed.

4.1. Micro-scale effects of compaction

The impact of compaction on changes in grain and pore geometry, size and distribution, at the micro scale, were examined by producing 3D and 2D images (slices) of the sand domain using the µCT (**Figure 2**). The 2D slices were randomly selected along the vertical axis of the columns,

425 and used to quantitatively analyze the different physical properties of pores and grains of the compacted and uncompacted samples. **Figure 3** presents the analysis process which was done for the 2D slices, in order to observe the changes in pore and sand grain properties following compaction at the top layer of the sample and at its bottom. **Figure 3a** shows representative images from: (i) an uncompacted sample (UN) at depth of 0-7 mm (**Figure 3a'**); (ii) the lower

430 part of the compacted sample (LC; depth of 9-18 mm) (**Figure 3a''**); and (iii) the top part of the compacted sample (TC; depth of 0-7 mm) (**Figure 3a'''**). In the UN, as well as in the LC domain, the sand grains are relatively round and uniform in size. By comparison, in TC, there are areas

18

with high proportion of relatively small and more angular grains, a result of the grains breakage in specific locations (marked by the yellow contours in **Figure 3a'''**, and also depicted

435 in **Figure 2**). Naturally, these changes in grain sizes also affect pore sizes and their spatial distribution, as visually observed in **Figure 2**, and depicted by the pores opening heat map (**Figure 3b**).

In **Figure 3c,** we demonstrate the changes in number of grains for a given area in the TC sample and the spatial distribution of these changes, in comparison to the UN and LC data. For this

440 purpose, each 2D scan, of any state and depth, was divided into a matrix of rectangles, 1.06 mm by 0.73 mm, each. In each rectangle, the number of sand grain centers was counted, and the rectangle was colored in accordance to the number of grain centers. In the presented images, the main colors for the LC and UN cases are blue and green, indicating about 3-4 grain centers per rectangle, with low variation in colors. However, for the TC case, there is a high

445 variation in the color of the rectangles, with a relatively high number of yellow and red rectangles (>6 grain centers) adjacent to green-blue rectangles.

The five randomly selected images of 'UN', 'TC', and 'LC' states were averaged and analyzed, as demonstrated in **Figure 3**, to provide a corresponding quantitative analysis of the number of grains per unit area, grain size (2D area) and pore opening (distance between adjacent

450 grains) (**Figure 4**). For simplicity, all of these values were normalized with respect to those corresponding to the UN state. In agreement with the visual observations, minor differences were measured with respect to the number of grains between the UN and LC states. However, a significant difference was measured with the TC samples, where the total number of grains, per unit area, was ~50% higher for TC compared to UN and LC (**Figure 4A**). Moreover, with

455 respect to changes in grain sizes, there is no significant difference between UN and LC, but for the TC layer, the average size of the grains was ~35% lower compared to UN and LC cases. The

same trend was measured also with respect to pore opening, as the pore average opening of

the TC was lower by ~10% compared to the two other cases.

(a) un-compacted (UN)   10 mm   (b) Compacted (TC)
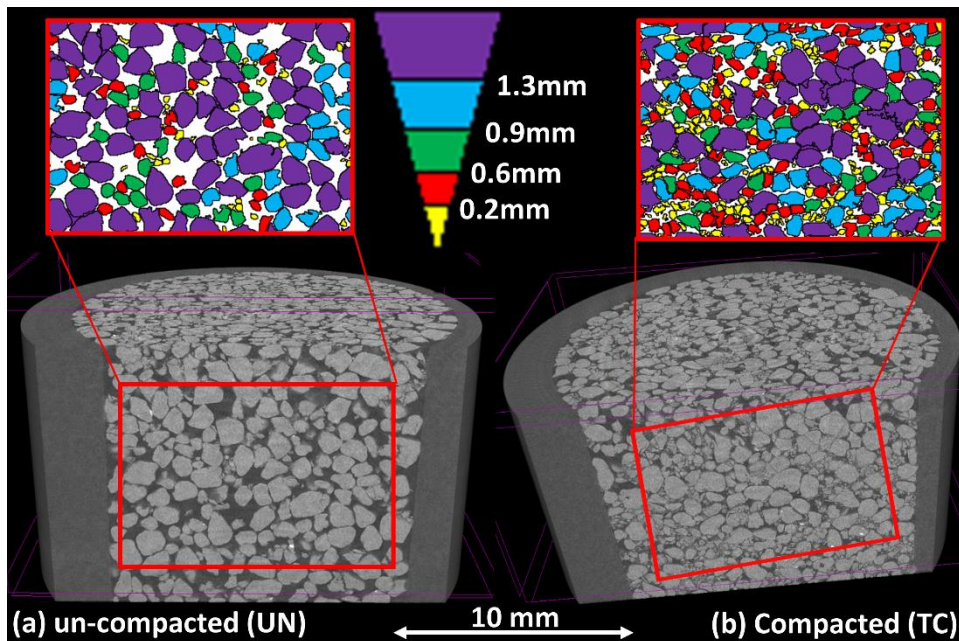
Figure 2: 3D visualization of the top ~10 mm of uncompacted (a) and compacted (b) sand samples. Red rectangles exemplify the cropping of the 2D slices off the 3D structure. The 2D colored slices present, visually, the different grain size distribution between the compacted and uncompacted samples. Grains sizes are in respect to the color-bar. In addition, it is seen in (b) that compaction reduced pores sizes, and increased grains angularity, due to breakage of the grains.
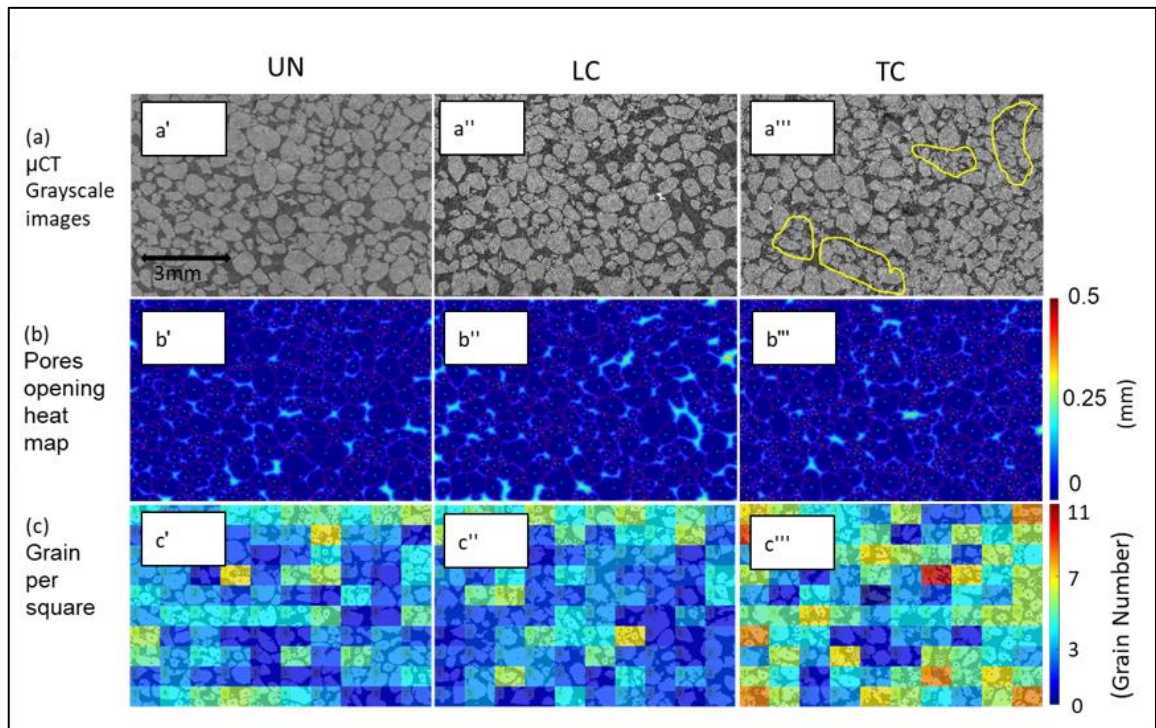

Figure 3: (a) µCT grayscale scan; (b) pore opening heat map; and (c) grain number spatial distribution map, for the uncompacted ('), low ('') and top (''') levels of compacted soil

samples, respectively. Yellow contours in (a''') indicate areas with high levels of grains
470   **breakage. In (b), the blue dots represent the grain centers and the color bar indicates the**
distance within the pores from the nearest grain. In (c), the rectangles are colored in
proportion to the number of grains in each one of them.

The analysis of the grain counting within the rectangles (**Figure 3c**) was also conducted for the

475   five randomly selected images. Analysis of each image was used to generate a histogram

describing how many rectangles contained the different numbers of grains (**Figure 4B**). For

the UN and LC cases grain density was lower compared to the TC setup, where the former had

on average 2-2.5 grains per rectangle, whereas the latter had 4 grains per rectangle.

Moreover, for the TC layers, in comparison with the LC and UN cases, the histogram shifts to

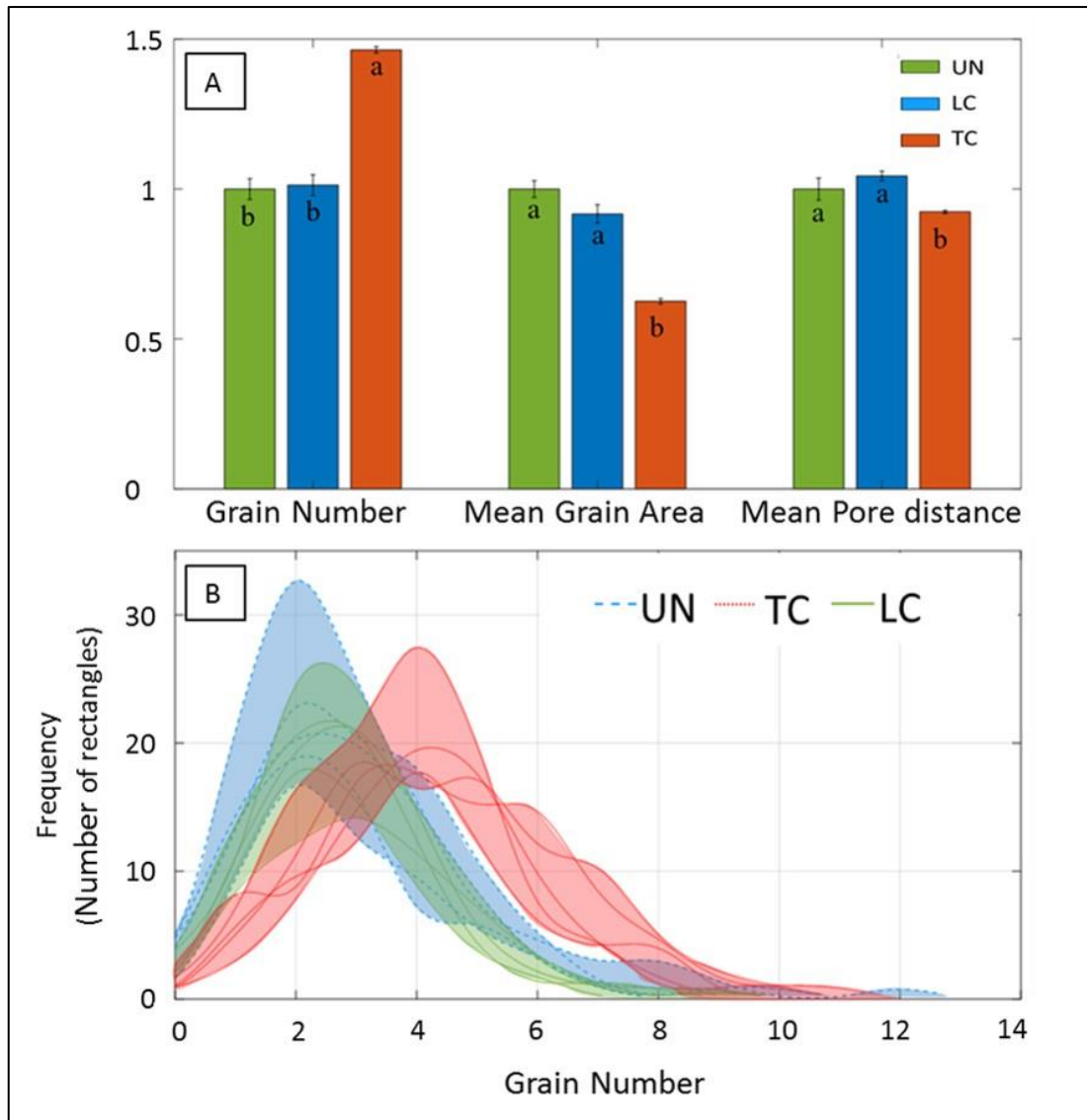480   the right, indicating a higher number of rectangles that contain 4 grains or more.

Figure 4: (A) Average grain number, average grain area and average pore distance of the uncompacted soil sample (UN), low (LC) and top (TC) levels of compacted soil samples. Measured values were normalized in respect to UN. **(B)** Histogram represents grain number distribution of the uncompacted soil samples, and low and top levels of the compacted soil samples. In (B), each line is the histogram of a single slice and the colored areas represent the range of the five measured histograms, for each state.

The presented image analyses, at the micro-scale, indicate the major impact that compaction has on the physical properties of the sand, close to the source of compaction (TC). It seems that compaction resulted in breakage due to friction of sand grains, leading to an increase in the grain number and their angularity, and a decrease in their mean size. In the deeper layer of the sand column (LC), the grains were practically not affected by the compaction and were similar to the control (UN) with respect to pore and grain sizes, shape and spatial distribution.

22

495   Moreover, it was shown that the compacted areas in the top layer were heterogeneously

distributed (**Figure 3c, 4B**), in agreement with the concept of preferential propagation of the

stress along the 'shear bands' (Nawaz et al., 2013; Naveed et al., 2016).

4.2. Macro-scale effects of compaction

At the macro scale, compaction effects were quantified by following the translocations of the

500   colored sand grains, in the 10-cm-long transparent column. The translocation of the sand

grains, ΔL [mm], was calculated by measuring the distance of selected grains from the

column's bottom at the initial state (L_0) and following compression (L_C), according to:

$$\Delta L = L_C - L_0. \tag{2}$$

Figure 5 presents ΔL along the soil profile. Maximal translocation was observed within the

505   upper layer of the soil profile, and it linearly decreases with depth, in agreement with the

results reported by Schlüter and Vogel (2016). However, it is important to remember that

translocation of the grains at each depth is the sum of all compaction processes that occurred

below the point of interest, and that it does not necessarily indicated the degree of

compaction (change of bulk density) at this point. In order to estimate the effect of

510   compaction on the bulk density along the soil profile we estimated the changes in distance

between adjacent grains, ΔD [mm], in a similar way that it was done for ΔL:

$$\Delta D = D_C - D_0 \tag{3}$$

where D_0 and D_C are the measured distances between any adjacent selected grains, before

and following compaction, respectively. Consequently, a negative ΔD value indicates

515   compaction and increase in bulk density, and vice versa.

Measurements of ΔD indicate that compaction was not uniform along the sand profile (**Figure

5**), showing that certain depths were more severely compacted. At depths of 6, 17, 36, and 60

mm, ΔD values were positive, indicating reduced bulk density at these specific locations.

Maximal compaction of ΔD = -1.3 mm was measured at a depth of 32 mm, followed by ΔD =

-1.1 mm at depth of 8 mm. Lower levels of the column were less compacted, excluding depths

of 68 and 82 mm where ΔD reached values of -1.0 and -0.8 mm, respectively.

This analysis further emphasizes the heterogeneous nature of soil compaction and the shear

band effect, as different locations along the profile were more compacted compare to others.

These differences are more notable at the macro scale, compared to the microscale

observations, from the CT experiments. Nevertheless, it is evident that most of the profile

underwent compaction, as most of the ΔD values are negative, and that maximal compaction

was at the top ~30 mm of the sample.
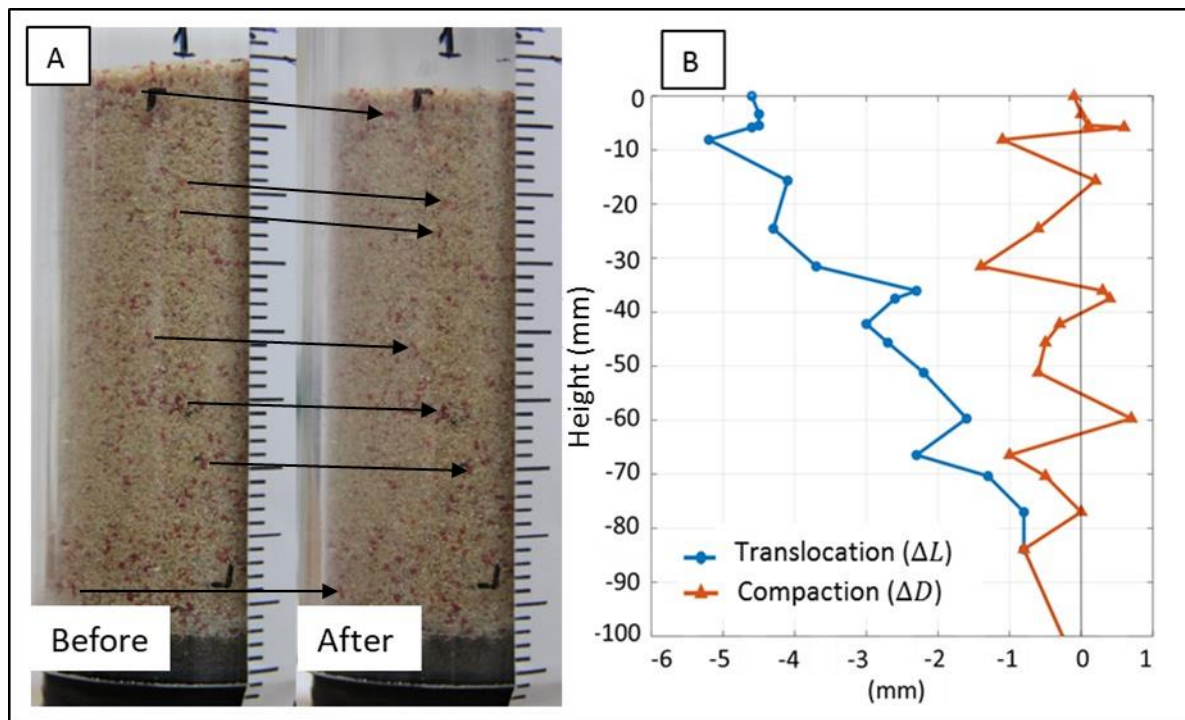
Figure 5: (A) photos of the examined sand column 'Before' and 'After' compaction. **Black arrows exemplify the vertical transition, due to compaction, of selected colored grains; (B)** measured changes in grains translocation and compaction along the sand column.

As seen from the micro and macro scales experiments, compaction induces the formation of

a non-uniform soil profile, with smaller pores, smaller grains, and higher bulk density at the

top levels of the soil profile, compared to the lower part of the profile. This structure is

opposed to typical natural conditions, where the lower soil levels are those with the higher

bulk density (Campbell, 1994; Hernanz et al., 2000). Consequently, important hydrological processes such as infiltration and evaporation may be altered due to compaction. These aspects will be discussed in the following sections, assuming that a layered structure of the matrix, with fine texture media, that overlies a coarse texture media, is analog to compacted

540 conditions.

4.3. Numerical model

The HYDRUS-1D model results showed similar trends to those proposed in the conceptual model and in the research hypothesis, including the unique pattern of drying from bottom to top, for the layered structure with the fine grains at the top. **Figure 6** presents temporal

545 changes in water content along the modeled domain and cumulative evaporation predicted by the model, for neutral - homogeneous setup (HO), and compacted setup with the finer pores and grains at the upper parts of the simulated domain (FU). The simulations were done for conditions of with and without the salt crust. As detailed above the simulations were ceased at the transition from S1 to S2.

550 From **Figure 6** it is seen that for salt free conditions, the FU setup sustained a longer S1 duration (~130 hours), compared to the HO setup (~72 hours). Consequently, cumulative evaporation during S1 of the FU setup was more than 40% higher, compared to the HO setup which shows a cumulative evaporation of ~2cm. The temporal changes in water content gives the physical explanation for that, showing that the FU structure maintains higher water

555 content levels at the upper soil layers due to the stronger capillary suction of these layers, which pump water from the lower levels, towards the evaporation front, at the soil surface.

Moreover, it is seen that while the addition of the modeled salt layer had a major impact on evaporation for the HO setup, its effect on the FU structure was more moderate. For the HO structure, the addition of the salt layer resulted in an immediate transition to S2, with a sharp

560 decrease in evaporation rate and reduced cumulative evaporation at the end of S1 by ~35%,

25

compared to the HO salt free setup (**Figure 6A**). For the FU structure, however, less noticeable changes in evaporation rates were observed following the addition of the salt layer, S1 sustained for additional ~48 hours, with the presence of the salt layer and the reduction in cumulative evaporation was of ~12% only (**Figure 6B**).

565   The disparity in the response to the added salt crust between the FU and HO setups point on the different hydraulic conditions between these two scenarios. At the HO state, the quick transition to S2 indicates on hydraulic discontinuity between the lower parts of the matrix and the overlying salt crust. This is demonstrated by the simulation results of pressure head and water content profiles in **Figure 7A-B** that present the low water content and high matric

570   suction of the HO profile, compare to the FU state. This resulted in a major reduction of the liquid water flux upward (**Figure 7C**), which enforced transition to S2 at the HO setup. At the compacted state, the higher capillary suction of the top layers, resulted in that even after two days of evaporation, the pressure head profile and water saturation of the top layers (**Figure 7A-B**) were conductive enough to support a hydraulic continuity between the matrix and the

575   added salt layer. Consequently, high liquid water fluxes were maintained for additional ~2 days, from the saturated matrix to the upper surface of the salt crust, where evaporation occurred.

While the numerical simulations strengthen the conceptual model and research hypotheses, validation of the model and the physical processes presented by the conceptual model is

580   essential due to the numerical model limitations. These limitations include the lack of precise and physically based information about the soil hydraulic properties in general and the salt layer in particular. Moreover, as detailed above, the HYDRUS-1D model is reliable as long as the hydraulic conditions permit to solve the Richards equation, which is not the case when the system moves into S2 evaporation. Therefore, the following column experiments were
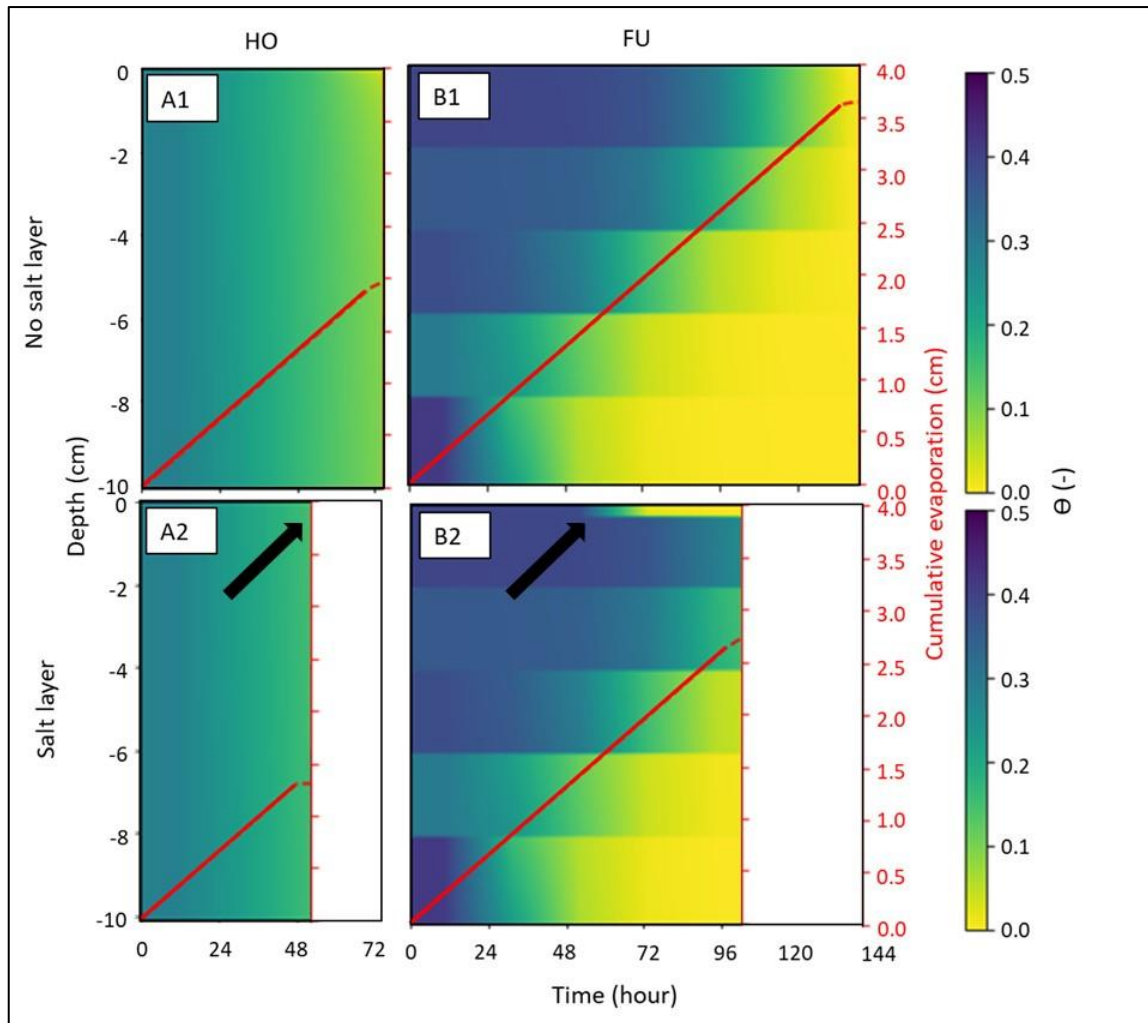
585   conducted.

Figure 6: HYDRUS-1D simulations for temporal changes in water content (heat map) and cumulative evaporation (red curves). The continuous line corresponds to S1 evaporation, and dashed line, to the transition into S2 evaporation. The black arrows indicate the time of the addition of the salt layer to the profile. (A) and (B) indicate on HO and FU setups, respectively. (1) and (2) indicate the conditions of non-saline, and saline setups, respectively.
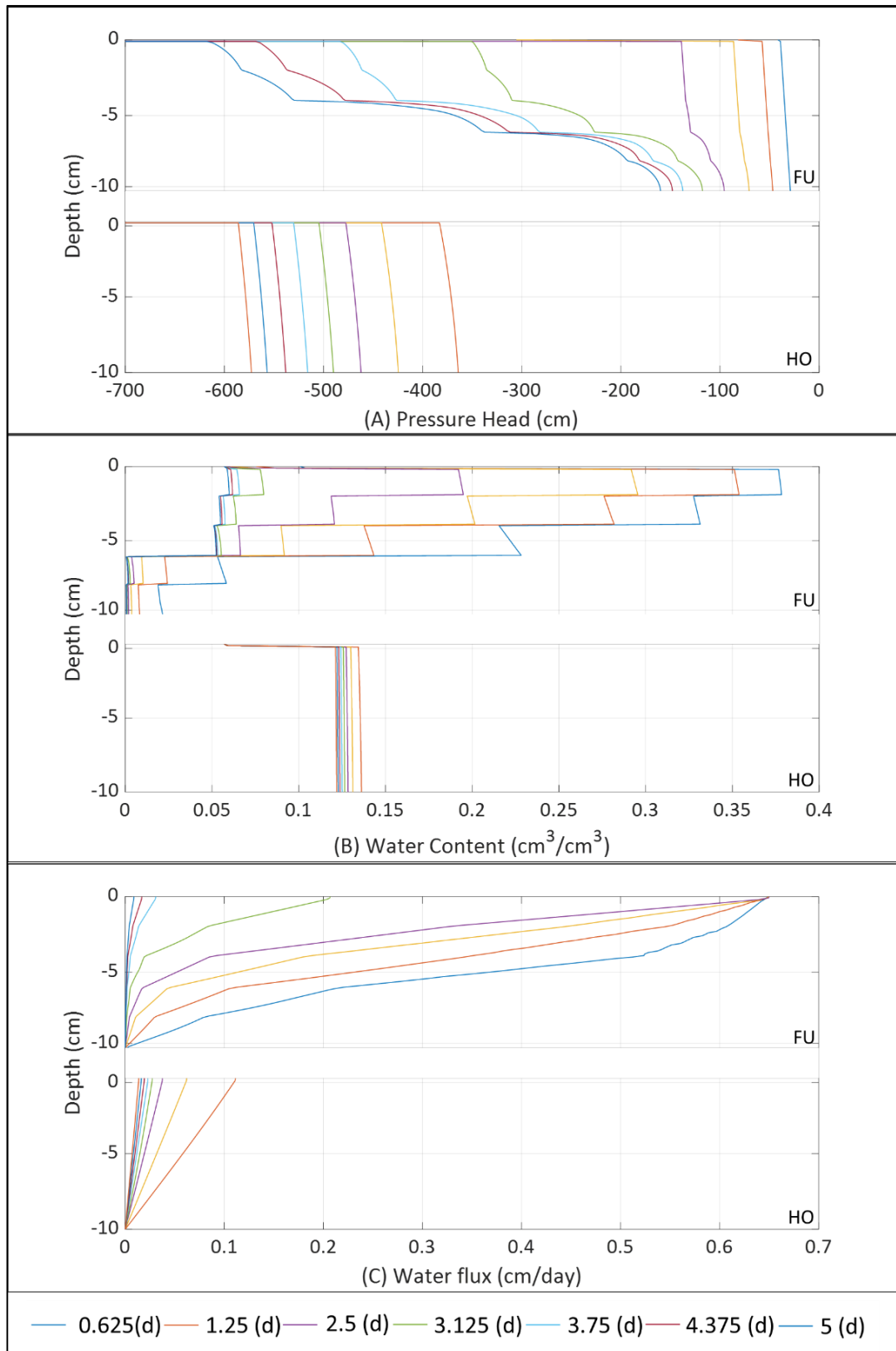
Figure 7: Profiled simulation results of pressure head (A); water content (B); and upward water flux (C) for compacted (FU), and uncompacted (HO) scenarios. Results are for different time steps after the addition of the salt crust.

595

28

4.4. Evaporation and salt precipitation in layered glass beads domain

As aforementioned, glass beads were used to fill the rectangular columns as detailed in **Table 1**, to represent the compacted conditions, and in a reverse order to mimic loose, e.g., tilled soil. The evaporation process during the column experiments of the three glass beads configurations saturated with the saline solution are represented by a set of pictures in **Figure 8**. It is possible to follow the movement of the drying front for the neutral homogeneous configuration (HO), and the compacted (FU) structures, which coincides with the numerical model results. Water flow and drying processes are also observed for the tilled (CU) setup.

For the HO structure, the evaporation front receded from top to bottom, as typically seen in evaporation of porous media. A notable efflorescence salt crust is observed, at the image of 54 hours (**Figure 8A**), yet it is important to emphasize that salt precipitation started at about 15 hours following evaporation onset.

For the FU structure, the soil surface remained moist for the entire duration of the experiment, while the drying front progressed upward, from bottom to top (**Figure 8B**). The unique drying pattern of the FU structure, which mimics compacted soil, is a result of the hydraulic properties of the top layer that had the highest capillary suction along the soil profile. This structure results in a continuous upward flow of the solution from the coarser layers at the bottom that have a lower capillary suction. A similar behavior was reported by Assouline and Narkis (2019) for DI water, where a detailed explanation of the impact of layered structure on evaporation is given. For the FU setup, under saline conditions, evaporation resulted in salt precipitation, at the soil surface, as observed in here at the image taken after 54 hours of evaporation (**Figure 8B**). As detailed for the HO set, salt precipitation initiated after about 15 hours.

For the CU structure, air penetration into the coarse upper layer was observed after 14 hours of evaporation and a slow recession of the evaporation front downward was observed over

625   time (**Figure 8C**). For the CU case, salt precipitation was minor, with no formation of a salt crust on the surface, or inside the medium.

Measurements and recording of changes in columns masses during the experiment enabled to compute average cumulative evaporation, of the different setups, as presented in **Figure 9.** Maximal values of standard deviation, for each setup, are detailed in **Table 2**. Transition from

630   S1 to S2, which is the time in which initial high and constant evaporation rate start to decrease, was marked on each cumulative evaporation curve in **Figure 9**. The transition times were determined by identifying the divergence of the curves from their tangents during initial stages of evaporation (see example for FU setup in **Figure 9**). The slope of each tangent line describes the initial (S1) evaporation rate of each curve.

635   For the HO, the duration of S1 with DI water was about 46 hours, with a cumulative evaporation of ~14 mm. Total evaporation after 300 hours for the HO, DI water, was 23 mm. The relatively long S1 duration and high cumulative evaporation for HO, resulted in the formation of a notable efflorescence salt crust (**Figure 8a**), with a thickness of about 3.5 mm as estimated from the images. The saline conditions reduced the duration of S1 by more than

640   70%, and cumulative evaporation at the transition from S1 to S2 was lowered by more than 80%, compared to evaporation from initially DI saturated columns.

In agreement with the observed drying pattern (**Figure 8b**), it was shown that FU S1 was the longest compared to all other setups (**Figure 9**). S1 duration for the FU structure was of 66 and 62 hours for the DI and saline conditions, respectively. Cumulative evaporation was also high

645   for the FU setup, with 11 and ~18 mm at the end of S1, for the saline solution and DI conditions, respectively, and total cumulative evaporation after 300 hours, of 26 mm for the saline solution, and 28 mm for the DI water. In comparison to the HO with DI water, the cumulative evaporation of the FU, after 300 hours, was 13% higher (**Figure 9**). The long duration of S1 for the FU, the persistence of the evaporation front at the surface of the

30

650   column, and the corresponding high cumulative evaporation (**Figure 9**), led to the

precipitation of a notable efflorescent salt crust (**Figure 8B**) with a thickness of about 6 mm as

estimated from the images.

While saline conditions for the HO setup led to reduction of more than 50% in total

evaporation and major changes in duration and cumulative evaporation of S1, for the FU

655   setup, the impact of salinity was much less prominent. For the FU, the salinity reduced

cumulative evaporation and the duration of S1 by less than 10%, and cumulative evaporation

at the transition from S1 to S2 was reduced by less than 40% (**Figure 9**).

Unlike for the HO setup, the evaporation from the CU column showed a transition from S1 to

S2 after ~19 hours of evaporation, and a cumulative evaporation of ~3.5 mm and ~4 mm

660   (**Figure 9**), for the saline solution and DI water, respectively. These results and the relatively

quick transition into S2, coincide with the receding of the drying front downward as seen in

Figure 8c. During S2, evaporation was minimal, due to the low rate of vapor diffusion through

the dry coarse porous medium at the surface, and total cumulative evaporation after 300

hours was 10 mm, for both saline and DI conditions, which is less than half the cumulative

665   evaporation of the HO setup and ~61% lower than the FU. As aforementioned, for the CU

saline conditions, no salt crust was observed because of the low cumulative evaporation, and

the receding evaporation front, that detained the processes of salinity buildup at the soil

surface. The absence of the salt crust at the surface of the CU column explains the observed

negligible difference in evaporation between the saline and DI water setups (**Figure 9**).
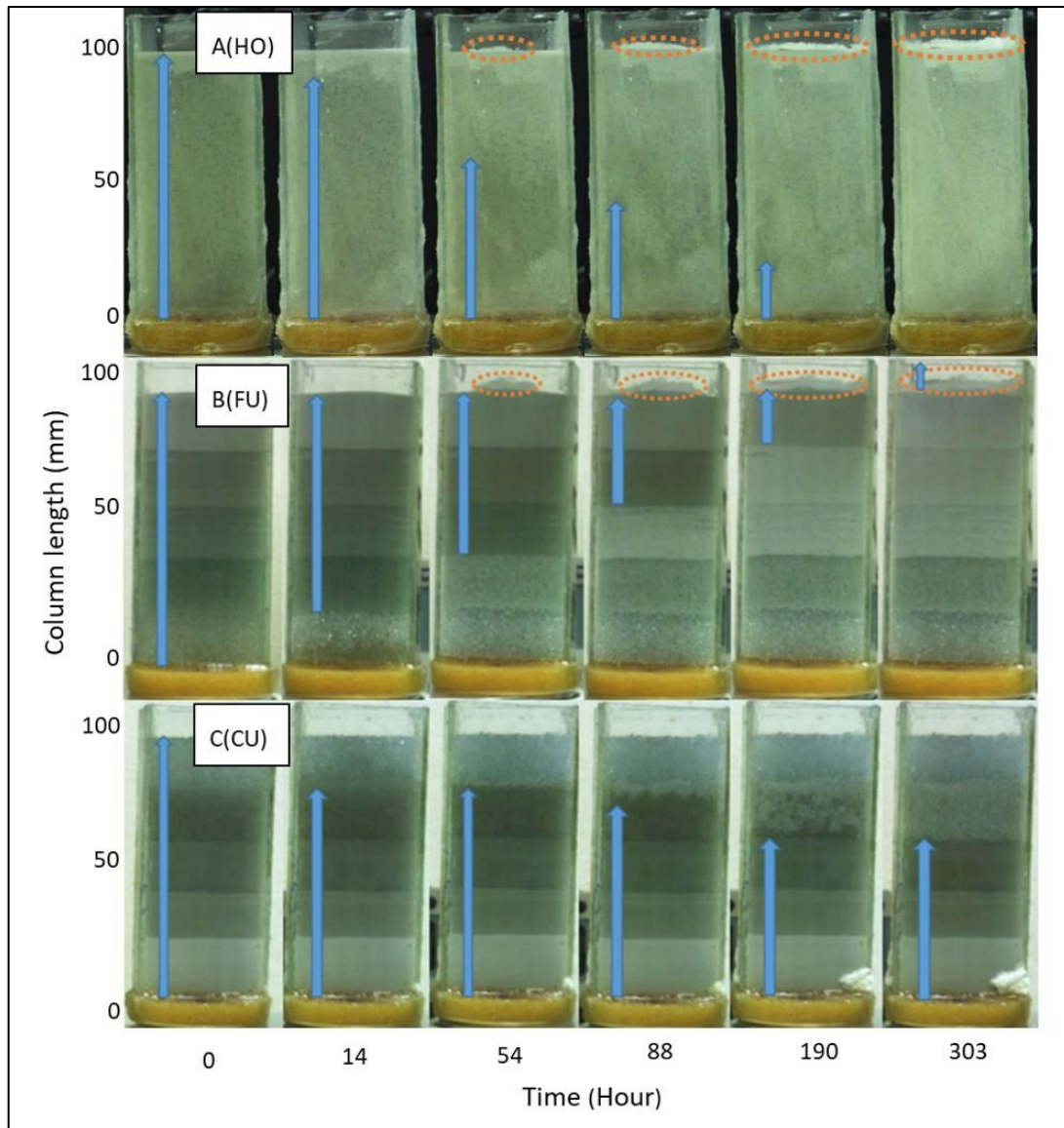
670

Figure 8: Evaporation and salt precipitation patterns for: (A) CU - with the coarse glass beads at the upper levels; (B) FU - with the fine glass beads at the upper levels; and (C) HO – homogeneous domain with the mixed glass beads. Numbers at the bottom indicate time length of evaporation. Top and bottom of the blue arrows indicate the upper and lower boundaries of the saturated zones, respectively. The orange circle marks locations of salt precipitation.

675
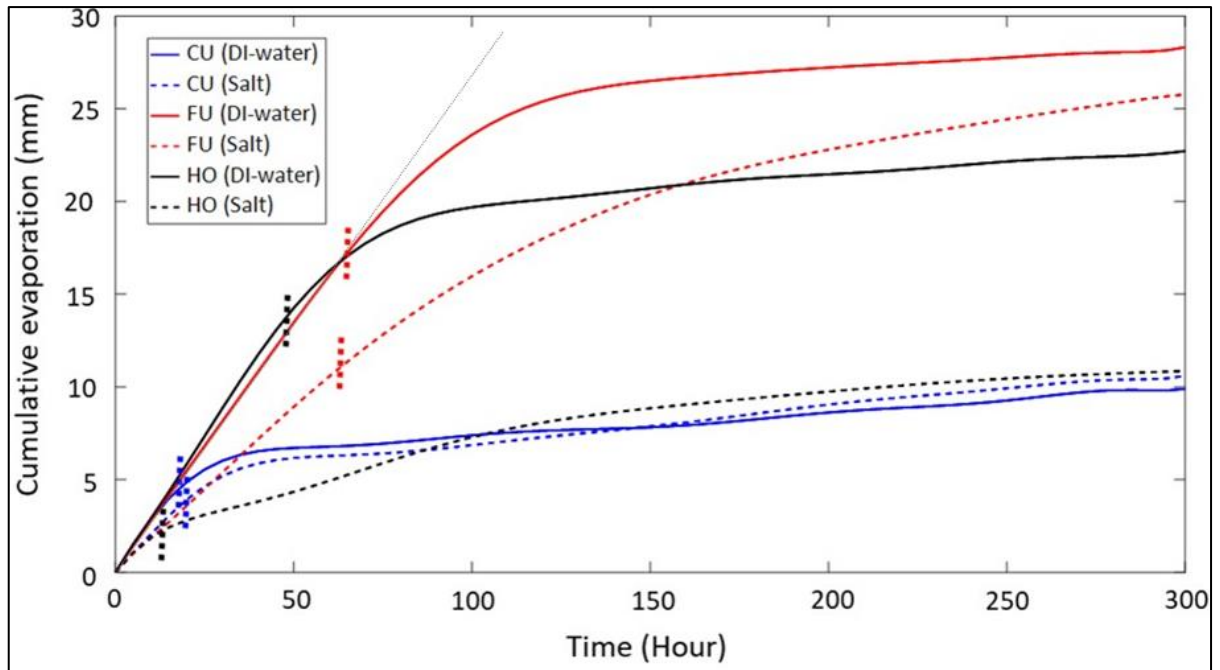
680

Figure 9: Cumulative evaporation for the coarse up (CU), fine up (FU), and the mixed (HO) structures, for conditions of DI water (solid lines) and saline solution (dashed lines). Vertical dotted lines indicate the transition from S1 to S2. Thin grey line is an example of a tangent line used to identify S1-S2 transition.

685

Table 2: Maximal values of standard deviation for cumulative evaporation measurements.

	DI - Water [mm]	Saline solution [mm]
HO	5.833	3.312
FU	5.928	4.957
CU	1.297	0.676

4.5. Differences in salinity impact on evaporation

690   As shown above, the three different setups: HO, FU, and CU, responded differently for the saline conditions, with the greatest impact observed for the HO, followed by the FU, and the CU that presented minimal changes. **Figure 10** presents the relative change in cumulative evaporation for the different setups, over time. After ~5 hours of evaporation, all setups presented a reduction of about 30% in cumulative evaporation compared to the DI conditions.

695   This reduction in evaporation may be a result of increased pore water NaCl concentration near the evaporation front at the surface of the columns, which results in reduction of the solution osmotic potential and vapor pressure. The 30% reduction coincides with the fact that vapor

33

pressure of a saturated NaCl solution, at 25 °C is equal to 2.401 kPa, which is ~25% lower than the vapor pressure of pure water that is equal to 3.169 kPa (Lide, 2007). However, more interestingly, after these first five hours, the relative impact of salinity on evaporation started to vary significantly, depending on the soil structural configurations.

 The HO setup introduced a reduction in evaporation that was much greater than 25%, at the order of 60%, throughout most of the evaporation process, with a maximal reduction of ~70% after about 50 hours. Total reduction in cumulative evaporation at the end of the experiment was around 50% (**Figure 10**). For the FU setup, the reduction in cumulative evaporation was maintained at 30-35% for about 100 hours, which is approximately 35 hours longer than S1 duration of the DI setup (~65 hours). After ~100 hours, the difference between the saline and DI setups for FU was gradually moderated, along S2, and by the end of the experiment, total cumulative evaporation of the saline FU setup was only 10% lower compared to the DI state (**Figure 10**). For the CU setup, after the initial reduction of ~30% at the first five hours of evaporation, the difference between the saline and DI conditions decreased, to very low values, and after 150 hours of evaporation, no differences were observed (**Figure 10**).

For both HO and FU setups, the greatest difference in evaporation between the DI and saline conditions was observed during the time where the DI columns were at S1 and the saline solution configurations moved into S2. The large difference between the DI and saline condition for the HO during this time, at the order of 70%, indicates that the reduction of the solution vapor pressure is not the only mechanism that reduces evaporation. For the non-saline condition the S1-S2 transition occurred after ~50 hours, for the HO setup. However, for the saline condition, S2 started after ~10 hours of evaporation only, with a minor cumulative evaporation at the order of 2mm.

From the HO-DI setup it is understood that at that time, the saline domain is moist enough to supply water to the upper atmosphere-domain interface and that S1 should be sustained.

Therefore, it is concluded that the transition into S2 after ~10 hours, is likely a result of increased osmotic potential of the solution, salt precipitation and the development of the efflorescent salt crust on top of the HO domain. The precipitated salt crust acts as a mulching layer that results in hydraulic discontinuity between the saturated domain and the atmosphere and vapor flow through the salt crust dictates the evaporation rate. This is in agreement with observations from previous studies (Gran et al., 2011; Nachshon and Weisbrod, 2015), and the numerical simulation.

For the FU setup, the fact that the differences in duration of S1 between the DI and saline conditions were minor (**Figure 9**), and the reduction in cumulative evaporation during S1 is at the order of 30-35%, suggests that the main mechanism that reduced evaporation was the reduction of the solution vapor pressure. The negligible impact of precipitated salt crust, for the FU setup, suggests that in this case the crust was hydraulically connected to the underlying media and that liquid water was flowing towards the surface of the salt crust, where the evaporation front was located. This hydraulic continuity suggests that the unique structure of the FU state, that mimics compacted soils, enables water from the lower layers of the drying profile to flow upward into and through the salt crust. It is suggested here that the hydraulic continuity between the precipitated salt crust and the underlying domain was possible for the FU and not for HO, due to the unique FU structure that keeps the upper layer of the domain wet.

For the CU setup, it is believed that during S1, the increase of the NaCl solution concentration at the evaporation front led to the observed reduction in evaporation at the order of 30%. This is in agreement with the vapor pressure reduction of a saturated NaCl solution. However, during S2 the differences between the DI and saline conditions decreased as vapor diffusivity, through the porous domain became the factor controlling evaporation, for both cases.

The differences in the impact of salinity on evaporation between the HO and FU setups (**Figures 9-10**), together with the differences in patterns of drying (**Figure 8**), support the research hypothesis that even though more salt accumulation on the surface is expected in compacted conditions, its impact on evaporation is expected to be moderate compared to neutral conditions, since the hydraulic connection to the surface persists longer and includes the salt crust. We suggest that, in the case of a homogeneous soil, the receding drying front breaks the hydraulic continuity to the salt crust. The water vapor diffusion process is therefore slowed down by the addition, on top of the soil surface, of the dry salt crust that acts as a mulching layer. For the FU setup, the high water content which is maintained at the soil surface throughout the evaporation process, sustains the hydraulic continuity from the saturated domain through the salt crust, towards its upper surface.
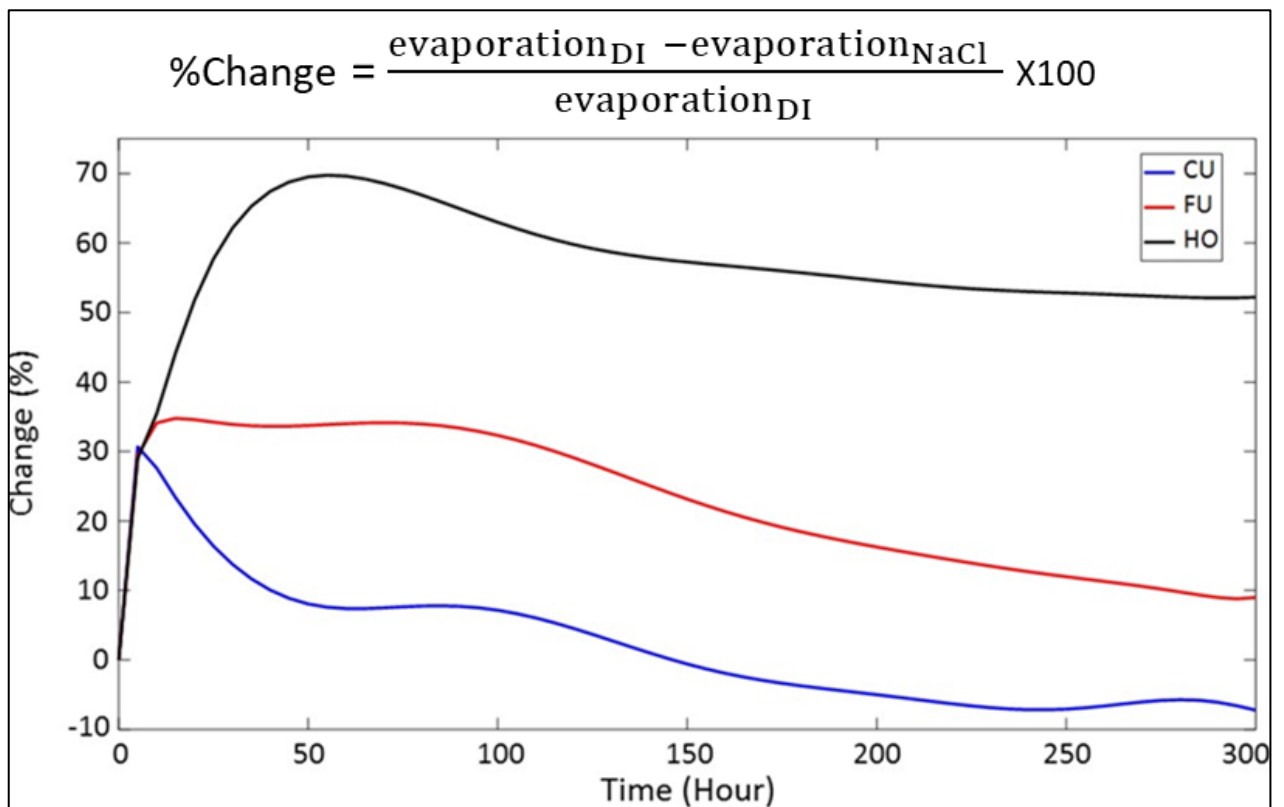
$$\%Change = \frac{evaporation_{DI} - evaporation_{NaCl}}{evaporation_{DI}} X100$$

Figure 10: **Relative difference in cumulative evaporation between saline and non-saline soil water solution over time, for the loose (CU), homogeneous (HO), and compacted (FU) setups.**

4.6. Sand column experiments

36

765   The glass beads experiments and the numerical model, supported the research hypothesis. However, both consisted of a layered structure, assuming it is a reasonable approximation for compacted conditions. The advantage of using the layered structure, with the fine texture media overlying coarser texture domains, is the simplicity of constructing the domain under controlled, accurate, and reproducible conditions. However, in reality, soil compaction will

770   form a more complex structure, as also shown here by the micro and macro scale compaction experiments (**sections 4.1 and 4.2**). Previous works also support the research hypotheses presented here in (Nassar and Horton, 1999; Sillon et al., 2003), yet the complex nature of soil structure following compaction, and the impact of salt precipitation on evaporation were ignored. Therefore, in order to associate the findings of the layered structure experiments and

775   simulation, with real life conditions, an experiments considering compacted and uncompacted sand columns were conducted.

Similarly to the numerical model simulations and the glass beads experiments, it is seen that the compacted sand, with no salt, had the highest cumulative evaporation with total evaporation of 20.0±0.23 mm (**Figure 11**). For the uncompacted sand, maximal cumulative

780   evaporation was equal to 16.9±3.11 mm. In respect to S1-S2 transition, in agreement with the layered structure results, it is seen that highest evaporation rate is measured for the DI compacted sand, with a notable reduction in evaporation rate observed after ~48 hours of evaporation, and cumulative evaporation of ~8 mm (**Figure 11**). For the uncompacted DI sand, transition into S2 with a notable reduction in evaporation rate was observed after ~25 hours

785   of evaporation, with cumulative evaporation of about 4.5 mm (**Figure 11**). For saline conditions the compacted sand also displayed higher cumulative evaporation compared to the uncompacted state, with total cumulative evaporation of about 16.5 mm and 14.5 mm, for the compacted and uncompacted samples, respectively (**Figure 11**). Also in agreement with the layered structure results, longest S1 were observed for the compacted conditions.

790
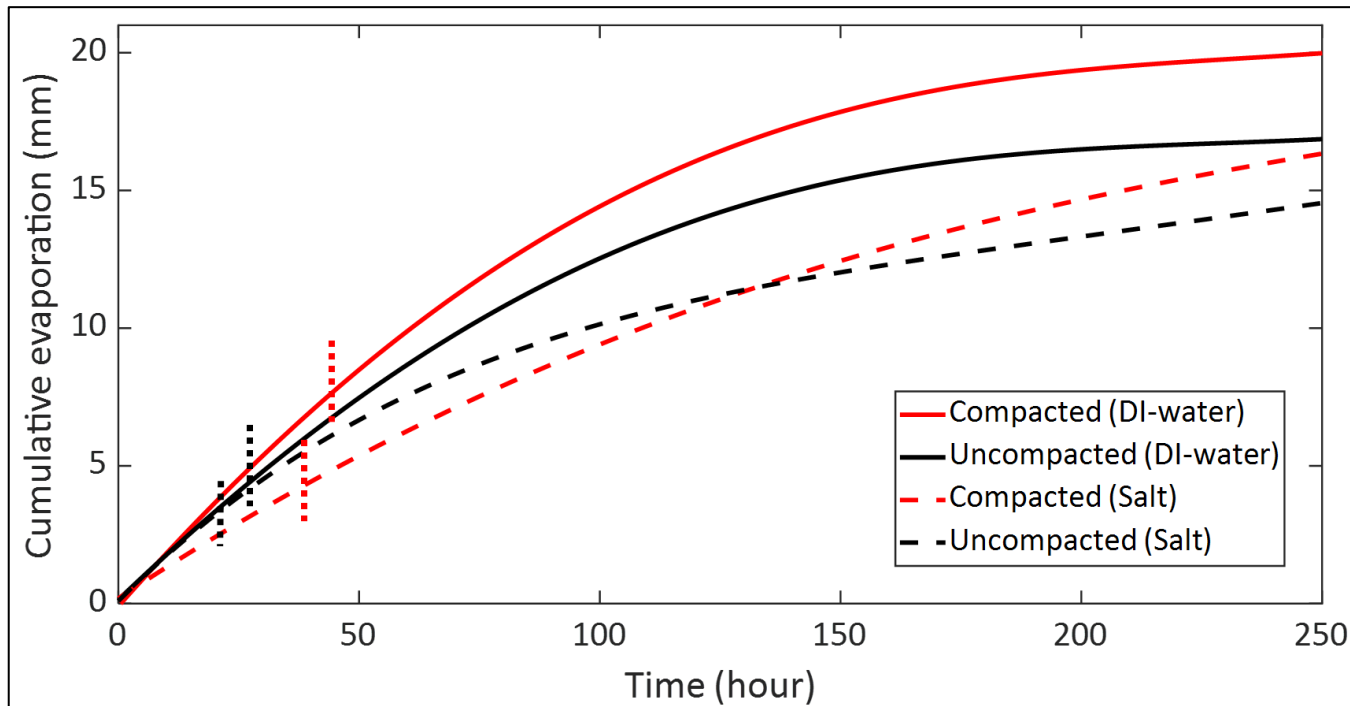
Figure 11: Cumulative evaporation for the compacted and uncompacted sand samples, for conditions of DI water (solid lines) and saline solution (dashed lines). Vertical dotted lines indicate the transition from S1 to S2.

795

5. Summary and Conclusions

This study investigates the effect of compaction on sand physical properties at the micro and macro scales, and its impact on evaporation combined with salt precipitation processes. Microscale properties such as the geometrical pore parameters were studied using X-ray computed micro-tomography (µCT) techniques by scanning sand samples before and after compaction. Compaction resulted in breakage of sand grains, reduced grain sizes, and pore average opening, mainly close to the source of compression. The spatial distribution of grain number, for the top levels of the compacted domain, has a higher proportion of areas with more grain numbers than the non-compacted and the lower levels of the compacted samples. These results illustrated the non-uniform spatial distribution of the physical changes that the

800

805

soil undergoes through compaction. The impact of compaction decreases with depth, away from the source of compression.

810   Macro-scale soil compaction changes were evaluated by analyzing images that captured the movement of colored sand grains and measuring their translocation before and after compaction. The highest translocation was at the upper levels of the soil profile, and with depth, translocation decreased. The distances between adjacent selected grains, before and following compaction, indicated that compaction is not uniform along the sand profile, with

815   certain levels compacted more than others, strengthening the assumption of the heterogeneous nature of soil compaction and the shear band effect.

Since compaction affects the particle arrangement along the profile in a non-uniform manner, with maximal compaction at the relatively high layers of the soil profile, the impact of compaction on combined evaporation and salt precipitation was observed using layered

820   columns packed with glass beads with increasing size with depth (FU). A reference setup consisted of a homogeneous column packed with mixed glass beads sizes (HO). In opposition to the compacted setup, a layered column where the glass beads sizes decreased with depth represented a tilled soil profile (CU). The cumulative evaporation measurements and the visual observations pointed to the significant impact of the different configurations on

825   combined processes of evaporation and salt precipitation.

For the HO structure, the drying front recedes from top to bottom. The relatively long S1 duration and high cumulative evaporation for the HO setup resulted in a notable precipitation of an efflorescence salt crust. The precipitated salt layer resulted in a sharp decrease in evaporation rate since hydraulic continuity to the surface is ceased, and the slow process of

830   vapor diffusion through the salt layer controls evaporation.

For the FU, the drying front propagated from bottom to top. S1 duration of the FU was long for the saline and DI water, and the cumulative evaporation was high, which led to prominent

efflorescent salt crust precipitation at the surface. However, in contrast to the HO, even though a notable salt layer was observed, its impact on evaporation at the FU structure was

835 moderated compared to its impact for the HO setup. This is attributed to the stronger capillary suction of the upper layers, at the FU structure, which pumps water from the underlying levels upwards, maintaining high saturation at the soil surface, which supports liquid water continuity from the soil to the evaporation front, at the salt crust upper surface.

For CU setup, a moderate recession of the evaporation front downward occurred over time

840 like in the HO configuration, and loss of hydraulic continuity to the surface was achieved relatively early. Thus, the cumulative evaporation was low, salt precipitation was minor and therefore negligible differences in evaporation between saline and non-saline conditions were observed.

This work sheds new light on the impact that soil compaction, which is a common feature in

845 arable lands, has on bare soil evaporation processes, for saline and non-saline conditions. Future studies should examine the findings of this study, under field conditions, for various soil textures, and to determine whether the observed phenomena occur in the field, where the 3-D expression of natural compaction will not necessarily create a layered soil profile. However, the insights gained from this study indicate that one may consider the use of

850 different agricultural practices to control the degree of soil compaction, to the benefit of the water regime in the root zone.

6. References

Akker, J.J.H., Canarache, A., 2001. Two European concerted actions on subsoil compaction.

855   Landnutzung und Landentwicklung 42, 15–22.

Alaoui, A., J. Lipiec, and H.H. Gerke. 2011. A review of the changes in the soil pore system due to soil deformation: A hydrodynamic perspective. Soil Tillage Res. 115–116: 1–15.

doi: 10.1016/j.still.2011.06.002.

Alaoui, A., M. Rogger, S. Peth, and G. Blöschl. 2018. Does soil compaction increase floods? A

860 review. J. Hydrol. 557(January): 631–642. doi: 10.1016/j.jhydrol.2017.12.052.

de Almeida, W.S., E. Panachuki, P.T.S. de Oliveira, R. da Silva Menezes, T.A. Sobrinho, et al.

2018. Effect of soil tillage and vegetal cover on soil water infiltration. Soil Tillage Res.

175(June 2017): 130–138. doi: 10.1016/j.still.2017.07.009.

Assouline, S. 2004. Rainfall-Induced Soil Surface Sealing: A Critical Review of Observations,

865 Conceptual Models, and Solutions. Vadose Zo. J. 3(2): 570–591. doi:

10.2136/vzj2004.0570.

Assouline, S. 2006a. Modeling the Relationship between Soil Bulk Density and the Hydraulic

Conductivity Function. Vadose Zo. J. 5(2): 697–705. doi: 10.2136/vzj2005.0084.

Assouline, S. 2006b. Modeling the Relationship between Soil Bulk Density and the Water

870 Retention Curve. Vadose Zo. J. 5(2): 554–563. doi: 10.2136/vzj2005.0083.

Assouline, S., and T. Kamai. 2019. Liquid and Vapor Water in Vadose Zone Profiles Above

Deep Aquifers in Hyper-Arid Environments. Water Resour. Res. 55(5): 3619–3631. doi:

10.1029/2018WR024435.

Assouline, S., and K. Narkis. 2019. Evaporation From Multilayered Heterogeneous Bare Soil

875 Profiles. Water Resour. Res. 55(7): 5770–5783. doi: 10.1029/2018wr024560.

Assouline, S., K. Narkis, R. Gherabli, P. Lefort, and M. Prat. 2014. Analysis of the impact of

surface layer properties on evaporation from porous systems using column

experiments and modified definition of characteristic length. doi: 10.1111/j.1752-

1688.1969.tb04897.x.

880 Assouline, S., and D. Or. 2006. Anisotropy factor of saturated and unsaturated soils. Water

Resour. Res. 42(12): 1–11. doi: 10.1029/2006WR005001.

Assouline, S., J.S. Selker, and J.Y. Parlange. 2007. A simple accurate method to predict time

of ponding under variable intensity rainfall. Water Resour. Res. 43(3): 1–10. doi:

41

10.1029/2006WR005138.

885   Augeard, B., S. Assouline, A. Fonty, C. Kao, and M. Vauclin. 2007. Estimating hydraulic

properties of rainfall-induced soil surface seals from infiltration experiments and X-ray

bulk density measurements. J. Hydrol. 341(1–2): 12–26. doi:

10.1016/j.jhydrol.2007.04.018.

Barik, K., E.L. Aksakal, K.R. Islam, S. Sari, and I. Angin. 2014. Spatial variability in soil

890   compaction properties associated with field traffic operations. Catena 120: 122–133.

doi: 10.1016/j.catena.2014.04.013.

Benson, C.H., I. Chiang, T. Chalermyanont, and A. Sawangsuriya. 2014. Estimating van

Genuchten Parameters α and n for Clean Sands from Particle Size Distribution Data.

From Soil Behavior Fundamentals to Innovations in Geotechnical Engineering. doi:

895   10.1061/9780784413265.033.

Berezniak, A., A. Ben-Gal, Y. Mishael, and U. Nachshon. 2018. Manipulation of Soil Texture to

Remove Salts from a Drip-Irrigated Root Zone. Vadose Zo. J. 17(1): 170019. doi:

10.2136/vzj2017.01.0019.

Bergstad, M., D. Or, P.J. Withers, and N. Shokri. 2017. The influence of NaCl concentration on

900   salt precipitation in heterogeneous porous media. Water Resour. Res. 53: 1702–1713.

doi: 10.1002/2016WR020060.

Bergstad, M., D. Or, P.J. Withers, and N. Shokri. 2018. Evaporation Dynamics and NaCl

Precipitation on Capillarity-Coupled Heterogeneous Porous Surfaces. Water Resour.

Res. 54(6): 3876–3885. doi: 10.1029/2018WR022614.

905   Bresson, L.M., C.J. Moran, and S. Assouline. 2004. Use of Bulk Density Profiles from X-

Radiography to Examine Structural Crust Models. Soil Sci. Soc. Am. J. 68(4): 1169–1176.

doi: 10.2136/sssaj2004.1169.

Brutsaert, W. 2005. Hydrology: An Introduction. Cambridge Univ. Press, New York.

Campbell, D.J. 1994. Determination and Use of Soil Bulk Density in Relation to Soil

910 Compaction. Dev. Agric. Eng. 11(C): 113–139. doi: 10.1016/B978-0-444-88286-8.50014-3.

Carman, P.C. 1937. Fluid flow through a granular bed. Transactions of the Institution of Chemical Engineers. : 15, 150–156.

Collins, T. J. 2007. ImageJ for microscopy. BioTechniques, 43(1): 25–27.

915 Dejong-Hughes, J., J. Moncrief, W.. Voorhees, and J.. Swan. 2001. soil compaction causes effects and control. : 1–16.

Gran, M., J. Carrera, S. Olivella, and M.W. Saaltink. 2011. Modeling evaporation processes in a saline soil from saturation to oven dry conditions. Hydrol. Earth Syst. Sci. 15(7): 2077–2089. doi: 10.5194/hess-15-2077-2011.

920 Hamza, M.A., and W.K. Anderson. 2005. Soil compaction in cropping systems: A review of the nature, causes and possible solutions. Soil Tillage Res. 82(2): 121–145. doi: 10.1016/j.still.2004.08.009.

Hendrickx, J.M.., and M. Flury. 2001. Uniform and preferential flow mechanisms in the vadose zone. Concept. Model. Flow Transp. Fract. Vadose Zo. Natl. Acad. Press.

925 Washington, D.C,: 149–187.

Hernanz, J.L., H. Peixoto, C. Cerisola, and V. Sánchez-Girón. 2000. An empirical model to predict soil bulk density profiles in field conditions using penetration resistance, moisture content and soil depth. J. Terramechanics 37(4): 167–184. doi: 10.1016/S0022-4898(99)00020-8.

930 Hillel, D. 1980. Introduction to Soil Physics. Academic Press, London.

Hopmans, J.W., A.S. Qureshi, I. Kisekka, R. Munns, S.R. Grattan, et al. 2021. Critical knowledge gaps and research priorities in global soil salinity.

Horn, R., H. Domial, A. Slowihka-Jurkiewiczb, and C. Van Ouwerkerkct. 1995. Soil compaction processes and their effects on the structure of arable soils and the environment.

935 Elsevier Sci. B.V.Soil Tillage Res. 35(35): 23–36. doi: 10.1016/0167-1987(95)00479-C.

Horton, R., M.. Ankeny, and R.. Allmaras. 1994. Effects of Compaction on Soil Hydraulic

Properties. Soil Compaction in Crop Production. p. 141–165

Kamai, T., and S. Assouline. 2018. Evaporation From Deep Aquifers in Arid Regions:

Analytical Model for Combined Liquid and Vapor Water Fluxes. Water Resour. Res.

940   54(7): 4805–4822. doi: 10.1029/2018WR023030.

Kasenow, M. 2002. Determination of hydraulic conductivity from grain size analysis. Water

Resources Publication, New York.

Keller, T., M. Lamandé, S. Peth, M. Berli, J.Y. Delenne, et al. 2013. An interdisciplinary

approach towards improved understanding of soil deformation during compaction. Soil

945   Tillage Res. 128: 61–80. doi: 10.1016/j.still.2012.10.004.

Keller, T., M. Sandin, T. Colombi, R. Horn, and D. Or. 2019. Historical increase in agricultural

machinery weights enhanced soil stress levels and adversely affected soil functioning.

Soil Tillage Res. 194(June). doi: 10.1016/j.still.2019.104293.

Kozeny, J. 1927. Uber kapillare Leitung des Wassers im Boden. Sitzungsber. Akad. Wiss. :

950   136, 271–306.

Lehmann, P., S. Assouline, and D. Or. 2008. Characteristic lengths affecting evaporative

drying of porous media. Phys. Rev. E - Stat. Nonlinear, Soft Matter Phys. 77(5): 1–16.

doi: 10.1103/PhysRevE.77.056309.

Lehmann, P., and D. Or. 2009. Evaporation and capillary coupling across vertical textural

955   contrasts in porous media. Phys. Rev. E - Stat. Nonlinear, Soft Matter Phys. 80(4): 1–13.

doi: 10.1103/PhysRevE.80.046318.

Lide, R.D. (ed.). 2007. CRC Handbook of Chemistry and Physics. CRC, Boca Raton.

Lipiec, J., and W. Stępniewski. 1995. Effects of soil compaction and tillage systems on uptake

and losses of nutrients. Soil Tillage Res. 35(1–2): 37–52. doi: 10.1016/0167-

960   1987(95)00474-7.

Mossadeghi-Björklund, M., J. Arvidsson, T. Keller, J. Koestel, M. Lamandé, et al. 2016. Effects

of subsoil compaction on hydraulic properties and preferential flow in a Swedish clay

soil. Soil Tillage Res. 156: 91–98. doi: 10.1016/j.still.2015.09.013.

Mossadeghi-Björklund, M., N. Jarvis, M. Larsbo, J. Forkman, and T. Keller. 2018. Effects of

965   compaction on soil hydraulic properties, penetration resistance and water flow

patterns at the soil profile scale (M. Goss, editor). Soil Use Manag. 35(3): 367–377. doi:

10.1111/sum.12481.

Nachshon, U. 2016. Seepage weathering impacts on erosivity of arid stream banks: A new

conceptual model. Geomorphology 261: 212–221. doi:

970   10.1016/j.geomorph.2016.03.011.

Nachshon, U. 2018. Cropland soil salinization and associated hydrology: Trends, processes

and examples. Water (Switzerland) 10(8). doi: 10.3390/w10081030.

Nachshon, U., E. Shahraeeni, D. Or, M. Dragila, and N. Weisbrod. 2011a. Infrared

thermography of evaporative fluxes and dynamics of salt deposition on heterogeneous

975   porous surfaces. Water Resour. Res. 47(12): 1–16. doi: 10.1029/2011WR010776.

Nachshon, U., and N. Weisbrod. 2015. Beyond the Salt Crust: On Combined Evaporation and

Subflorescent Salt Precipitation in Porous Media. Transp. Porous Media 110(2): 295–

310. doi: 10.1007/s11242-015-0514-9.

Nachshon, U., N. Weisbrod, M.I. Dragila, and A. Grader. 2011b. Combined evaporation and

980   salt precipitation in homogeneous and heterogeneous porous media. Water Resour.

Res. 47(3): 1–16. doi: 10.1029/2010WR009677.

Nassar, I.N., and R. Horton. 1997. Heat, Water, and Solute Transfer in Unsaturated Porous

Media: I - Theory Development and Transport Coefficient Evaluation. Transp. Porous

Media 27(1): 17–38. doi: 10.1023/A:1006583918576.

985   Nassar, I.N., and R. Horton. 1999. Salinity and compaction effects on soil water evaporation

and water and solute distributions. Soil Sci. Soc. Am. J. 63(4): 752–758. doi:

10.2136/sssaj1999.634752x.

990 Naveed, M., P. Schjønning, T. Keller, L.W. de Jonge, P. Moldrup, et al. 2016. Quantifying vertical stress transmission and compaction-induced soil structure using sensor mat and X-ray computed tomography. Soil Tillage Res. 158(October 2017): 110–122. doi: 10.1016/j.still.2015.12.006.

Nawaz, M.F., G. Bourrié, and F. Trolard. 2013. Soil compaction impact and modelling. A review. Agron. Sustain. Dev. 33(2): 291–309. doi: 10.1007/s13593-011-0071-8.

Or, D., P. Lehmann, E. Shahraeeni, and N. Shokri. 2013. Advances in Soil Evaporation Physics-
995 A Review. Vadose Zo. J. 12(4): vzj2012.0163. doi: 10.2136/vzj2012.0163.

Or, D., P. Lehmann., and N. Shokri, N. 2007. Characteristic lengths affecting evaporation from heterogeneous porous media with sharp textural boundaries. Estudios de la Zona No Saturada del Suelo, 8, 1-8.

Otsu, N. 1979. A Threshold Selection Method from Gray-Level Histograms. IEEE Trans. Syst.
1000 Man. Cybern. 9(1): 62–66. doi: 10.1109/TSMC.1979.4310076.

Pagliai, M., A. Marsili, P. Servadio, N. Vignozzi, and S. Pellegrini. 2003. Changes in some physical properties of a clay soil in Central Italy following the passage of rubber tracked and wheeled tractors of medium power. Soil Tillage Res. 73(1–2): 119–129. doi: 10.1016/S0167-1987(03)00105-3.

1005 Piotrowski, J., J.A. Huisman, U. Nachshon, A. Pohlmeier, and H. Vereecken. 2020. Gas permeability of salt crusts formed by evaporation from Porous media. Geosci. 10(11): 1–19. doi: 10.3390/geosciences10110423.

Podder, M., M. Akter, A. S. M. Saifullah, and S. Roy. 2012. Impacts of plough pan on physical and chemical properties of soil. Journal of Environmental Science and Natural
1010 Resources. 5(1), 289-294.

Prat, M. 2002. Recent advances in pore-scale models for drying of porous media. Chem. Eng. J. 86(1–2): 153–164. doi: 10.1016/S1385-8947(01)00283-2.

Rad, M.N., and N. Shokri. 2012. Nonlinear effects of salt concentrations on evaporation from

46

porous media. Geophysical research letters, 39(4).doi: 10.1029/2011GL050763.

1015   Rasmussen, K.J. 1999. Impact of ploughless soil tillage on yield and soil quality: A

Scandinavian review. Soil Tillage Res. 53(1): 3–14. doi: 10.1016/S0167-1987(99)00072-

0.

Reicosky, D.C., W.B. Voorhees, and J.K. Radke. 1981. Unsaturated Water Flow Through a

Simulated Wheel Track1. Soil Sci. Soc. Am. J. 45(1): 3. doi:

1020   10.2136/sssaj1981.03615995004500010001x.

Schlüter, S., and H.J. Vogel. 2016. Analysis of soil structure turnover with garnet particles and

X-Ray microtomography. PLoS One 11(7): 1–17. doi: 10.1371/journal.pone.0159948.

Shah, A.N., M. Tanveer, B. Shahzad, G. Yang, S. Fahad, et al. 2017. Soil compaction effects on

soil health and cropproductivity: an overview. Environ. Sci. Pollut. Res. 24(11): 10056–

1025   10067. doi: 10.1007/s11356-017-8421-y.

Shokri-kuehni, S.M.S., M. Norouzi, C. Webb, N. Shokri, C. Zeiss, et al. 2017. Impact of type of

salt and ambient conditions on saline water evaporation from porous media. Advances

in Water Resources, 105: 154–161. doi: 10.1016/j.advwatres.2017.05.004.

Shokri-Kuehni, S.M.S., T. Vetter, C. Webb, and N. Shokri. 2017. New insights into saline water

1030   evaporation from porous media: Complex interaction between evaporation rates,

precipitation, and surface temperature. Geophys. Res. Lett. 44(11): 5504–5510. doi:

10.1002/2017GL073337.

Shokri, N., P. Lehmann, and D. Or. 2010. Evaporation from layered porous media. J. Geophys.

Res. Solid Earth 115(6): 1–12. doi: 10.1029/2009JB006743.

1035   Sillon, J.F., G. Richard, and I. Cousin. 2003. Tillage and traffic effects on soil hydraulic

properties and evaporation. Geoderma 116(1–2): 29–46. doi: 10.1016/S0016-

7061(03)00092-2.

Shokri, N., P. Lehmann, P. Vontobel, and D. Or. 2008. Drying front and water content

dynamics during evaporation from sand delineated by neutron radiography. Water

1040   resources research, 44(6).

Šimůnek, J., A. M. Šejna, H. Saito, M. Sakai, and M.T. Van Genuchten. 2013. The HYDRUS-1D software package for simulating the movement of water, heat, and multiple solutes in variably saturated media, version 4.17. HYDRUS Softw. Ser. 3D (June): 343.

Soane, B.D., and C. van Ouwerkerk. 1995. Implications of soil compaction in crop production

1045   for the quality of the environment. Soil Tillage Res. 35(1–2): 5–22. doi: 10.1016/0167-1987(95)00475-8.

El Titi, A. 2003. Soil Tillage in Agroecosystems. CRC Press, Boca Raton/London/New York/Washington D.C.

Wang, J.-P., N. Hu, B. Françoise, and P. Lambert. 2017. Estimating water retention curves and

1050   strength properties of unsaturated sandy soils from basic soil gradation parameters. Water Resour. Res. 53: 6069–6088. doi: 10.1002/2017WR020411.Received.

Weisbrod, N., U. Nachshon, M. Dragila, and A. Grader. 2013. Micro-CT Analysis to Explore Salt Precipitation Impact on Porous Media Permeability. : 231–241. doi: doi:10.1007/978-94-007-7534-3_20.

1055 Yakirevich, A., N. Weisbrod, M. Kuznetsov, C.A. Rivera Villarreyes, I. Benavent, et al. 2013. Modeling the impact of solute recycling on groundwater salinization under irrigated lands: A study of the Alto Piura aquifer, Peru. J. Hydrol. 482: 25–39. doi: 10.1016/j.jhydrol.2012.12.029.

Zhou, T., J. Šimůnek, and I. Braud. 2021. Adapting HYDRUS-1D to simulate the transport of

1060   soil water isotopes with evaporation fractionation. Environmental Modelling & Software, 143, 105118.